iScience

CellPress
OPEN ACCESS

Review

Hybridized Nanogenerators for Multifunctional Self-Powered Sensing: Principles, Prototypes, and Perspectives

Tingting Zhang,[1,2,3] Zhen Wen,[1,*] Yina Liu,[4] Zhiyuan Zhang,[4] Yongling Xie,[3,*] and Xuhui Sun[1,*]

SUMMARY

Sensors are a key component of the Internet of Things (IoTs) to collect information of environments or objects. Considering the tremendous number and complex working conditions of sensors, multifunction and self-powered feathers are two basic requirements. Nanogenerators are a kind of devices based on the triboelectric, piezoelectric, or pyroelectric effects to harvest ambient energy and then converting to electricity. The hybridized nanogenerators that combined multiple effects in one device have great potential in multifunctional self-powered sensors because of the unique superiority such as generating electrical signals directly, responding to diverse stimuli, etc. This review aims at introducing the latest advancements of hybridized nanogenerators for multifunctional self-powered sensing. Firstly, the principles and sensor prototypes based on TENG are summarized. To avoid signal interference and energy insufficiently, the multifunctional self-powered sensors based on hybridized nanogenerators are reviewed. At last, the challenges and future development of multifunctional self-powered sensors have prospected.

INTRODUCTION

With the construction of smart cities and the gradual improvement of big data, the IoTs has obtained booming development in the past few years (Ullah et al., 2020; Oztemel and Gursev, 2020; Berglund et al., 2020). Nowadays, the application of the IoTs involves various aspects including, but not limited to, industry (Li, 2019), agriculture (Chen and Yang, 2019), environment protection (Xu et al., 2019), transportation (Jin et al., 2020), logistics (Guo, 2017), security (Tschofenig and Baccelli, 2019), and other infrastructure fields (Verma et al., 2019; Salahuddin et al., 2017; Chang et al., 2017). More importantly, the IoTs also holds essential potential and exudes unique brilliance in some emerging fields such as household (Liegeard and Manning, 2020), healthcare (Gardasevic et al., 2020), education (Abdel-Basset et al., 2019), finance (Abbasi et al., 2019), and services (Gil et al., 2016). The mighty rising of IoTs effectively promotes the intelligent development of these aspects and makes the use and distribution of limited resources more reasonable, thus improving the efficiency and benefit of the industry. In general, the basic framework of IoTs can be divided into three levels: perception layer, network layer, and application layer (Tao et al., 2014; Jing et al., 2014). The different levels are relatively independent but mutually supportive and contribute to the realization of the IoTs together.

As the indispensable element of the perception layer, sensors are the foundation and premise of the IoTs realization (Yu and Li, 2019; Voas, 2016; Pradilla et al., 2018). The major function of sensors is to probe information about the environment or objects and transmit that information to the background through the network for processing (Potyrailo, 2016; Mikusz et al., 2015; Ferrandez-Pastor et al., 2016). Enormous efforts have been devoted to the development of various sensors such as response to the motion (Liu et al., 2018), pressure (Ruth et al., 2020), temperature (E et al., 2019), humidity (Duan et al., 2019), chemical (Grover and Lall, 2020), etc. However, the IoTs is an extremely complex system especially considering the connection of human, machine, and environmental surroundings. Thus, it is an ordinary condition that detects multiple signal factors simultaneously and becomes the original purpose of the research on multifunctional sensors (MS). The MS mainly relates to a device that senses two or more measurements at the same time and converts them into electrical or other form signals that can be received and processed (Xie et al., 2019; Tokuda et al., 2010; Majumder et al., 2019).

[1]Institute of Functional Nano and Soft Materials (FUNSOM), Jiangsu Key Laboratory for Carbon-Based Functional Materials and Devices, Soochow University, Suzhou 215123, China

[2]School of Nano Technology and Nano Bionics, University of Science and Technology of China, Hefei 230026, China

[3]Inkjet Printing Technology Research Center, Printable Electronics Research Center, Suzhou Institute of Nano-tech and Nano-bionics, Chinese Academy of Sciences, Suzhou 215123, China

[4]School of Advanced Technology, School of Science, Xi'an Jiaotong-Liverpool University, Suzhou 215123, China

*Correspondence: wenzhen2011@suda.edu.cn (Z.W.), ylxie2013@sinano.ac.cn (Y.X.), xhsun@suda.edu.cn (X.S.)

https://doi.org/10.1016/j.isci.2020.101813

Although the characteristic of multifunction is an essential requirement, there is another bottleneck need to be seriously considered, that is, power supply (Han et al., 2018a; Watral and Michalski, 2013; Mandourarakis and Koutroulis, 2018; Tanaka et al., 2011). Once the IoTs start working, they need to operate sustainably and uninterrupted (Atzori et al., 2010). There is no doubt that powers are indispensable for sensing, signal transmission, and processing (Stankovic, 2014; Al-Fuqaha et al., 2015). The traditional energy provider is usually batteries that are rigid and even worse is that frequent charging and replacement are also common practices (Ma and Yang, 2006; Kuncoro et al., 2019; Chau et al., 2010). In another aspect, considering that a large number of sensors are used in harsh environments or remote areas, it will consume a lot of manpower, material, and financial resources if battery power is used. Those drawbacks dramatically hinder further application for the sensors in IoTs. Therefore, developing multifunctional self-powered sensors (MSPS) is of great significance and highly desirable.

In 2006, Wang's group firstly proposed piezoelectric nanogenerator (PENG) relying on the zinc oxide nanowire array that can convert nanoscale mechanical energy into electrical energy (Wang and Song, 2007). Later, the triboelectric nanogenerator (TENG) and pyroelectric nanogenerator (PyENG) were introduced one after the other in 2012 (Fan et al., 2012a; Yang et al., 2012). Precisely speaking, nanogenerators are a kind of device that converts external stimulations into electrical signal based on the triboelectric, piezoelectric, or pyroelectric effects (Indira et al., 2019; Proto et al., 2017). TENG has the feature of high voltage and low current output, PENG output voltage is high and current is small, whereas PyENG output characteristics are also different from them (Chen et al., 2017). When integrating them, the output signals will inevitably overlap or even cover each other. It is rather difficult to distinguish the respective signals if there is a common back-end processing system. Even though the output characteristics of these three nanogenerators are different, an independent signal receiving and processing system for each nanogenerator can be exploited to avoid signals interference. Because the nanogenerators can harvest energy from the environments and generate electrical signals directly under the external stimuli, unlike the traditional sensors that need an extra power supply, it is entirely suitable for the realization of self-powered sensors (Fan et al., 2016; Khan et al., 2019; Askari et al., 2018). In addition, the nanogenerators respond to a lot of factors with proper materials adoption and structure design that possess the unique feather of multifunctionality (Park et al., 2016; Lai et al., 2019; He et al., 2020). More importantly, by integrating two or more kinds of effects in one device, the hybridized nanogenerators (HNG) provide an excellent solution for monitoring multiple external stimuli simultaneously with the advantages of making up for the insufficient energy and avoiding signal interference when detecting multiple parameters (Yang et al., 2018, 2020; Ma et al., 2020). In other words, the HNG is the best choice for the multifunctional self-powered sensors until now (Kim et al., 2017; Wang et al., 2016; Zhao et al., 2018). Nevertheless, there has not been a review summarizing the progress on the multifunctional self-powered sensors based on the HNG yet.

In this review, we systematically introduced and summarized the latest progress on the multifunctional self-powered sensor based on the HNG. Figure 1 schematically presents an overview of this topic. Firstly, we introduced the principles and prototypes of multifunctional self-powered sensors based on the TENG. Particularly, the material selection to fabricate TENG is quite extensive, and the structure design is very flexible with four working modes, which ensure the ability to detect various stimuli even though there is only a single TENG device (Lin et al., 2018; Guo et al., 2017; Ahmed et al., 2019). However, there still some issues that are not solved for single TENG sensing. On the one hand, the energy harvesting by TENG is not sufficient sometimes for the signal transmission and processing in the application of IoTs, so strictly speaking, the system cannot be self-powered. On the other hand, signal interference is inevitable when sensing multiple parameters simultaneously because all the signals are generated by the single TENG. In view of the two drawbacks, developing the hybrid nanogenerators for multifunctional self-powered sensors is extremely important (Ma et al., 2017; Singh and Khare, 2018; Jiang et al., 2020). Hence, in the subsequent section, multifunctional sensors based on binary and multiple effects will be summarized. Finally, we concluded the review and prospect of the challenges and future development of sensors in the IoTs.

TENG-BASED MULTIFUNCTIONAL SELF-POWERED SENSORS

Principles

The triboelectrification is a common phenomenon in external environment or activities in our daily life but it often causes a negative effect such as an explosion, fire, electrostatic shock, or signal interference (Jian et al., 2009, 2010; Greason, 2012; Byun et al., 2016). No one had tried to exploit the electric energy from friction until TENG was proposed by Wang's group in 2012 (Fan et al., 2012a). As illustrated in Figure 2A,

Figure 1. Overview of Hybridized Nanogenerators for Multifunctional Self-Powered Sensing

Reproduced with permission (Wu et al., 2019b). Copyright©2018, Wiley-VCH. Reproduced with permission (Wang et al., 2020b). Copyright©2018, American Chemical Society. Reproduced with permission (Zhu et al., 2020b). Copyright©2020, Elsevier. Reproduced with permission (Zhang et al., 2018). Copyright©2018, Wiley-VCH. Reproduced with permission (Shin et al., 2020). Copyright©2020, Elsevier. Reproduced with permission (Song et al., 2019). Copyright©2019, Wiley-VCH. Reproduced with permission (Zhao et al., 2020). Copyright©2020, Elsevier. Reproduced with permission (Zhao et al., 2018). Copyright©2018, Elsevier.

they employed the PET and Kapton polymer sheets as friction layers, with Au alloy film coated on the back-side of them, respectively. The mechanism is displayed in Figure 2B. At the original state, PET and Kapton are separated from each other. In view of the charge affinity difference of two friction layers, the negative and positive charges are going to be generated on their surface if they are contacted with each other by the applied external force. Once releasing the force, the charges with opposite polarity will be induced on the electrodes and build a potential difference. If a complete electrical circuit is formed by the load, the current signal will create for screening out the electric field. In short, the TENG relies on the principles of electrification and electrostatic induction (Wu et al., 2019a). More importantly, a consecutive alternating electrical signal will be detected if the contact-separation process alternates to form the repeating cycle (Lin et al., 2016; Chen et al., 2020). After putting forward the TENG with contact-separation (CS) mode, the other types are also designed in succession, including lateral-sliding (LS) mode, single-electrode (SE) mode, and freestanding triboelectric-layer (FS) mode (as can be seen in Figure 2C) (Wang, 2015).

In addition to qualitative analysis, the TENG can also be theoretically explained, which originates from the equation of Maxwell's displacement currents (Wang, 2017):

$$J_D = \frac{\partial D}{\partial t} = \varepsilon \frac{\partial E}{\partial t} + \frac{\partial P_S}{\partial t} \qquad \text{(Equation 1)}$$

where $\boldsymbol{D}$ is the displacement field, ε is the permittivity of the dielectric materials, $\boldsymbol{E}$ stands for the electric field, and $\boldsymbol{P_S}$ is the polarization intensity. The polarized charge that can be caused by the triboelectric,

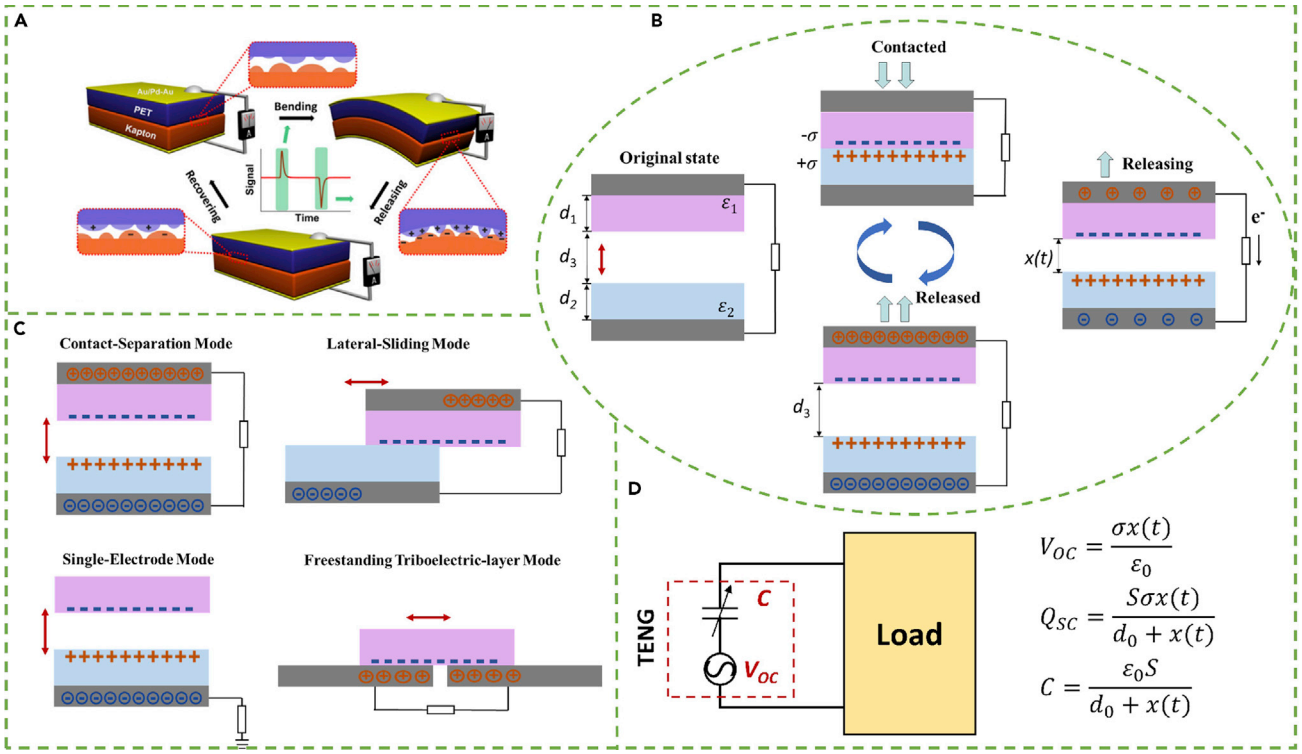

Figure 2. Mechanism of TENG

(A) Schematic diagram of the first proposed TENG. Reproduced with permission (Fan et al., 2012a). Copyright©2012, Elsevier.

(B) Working mechanism of contact-separation mode TENG. Reproduced with permission (Wang, 2017). Copyright©2017, Elsevier.

(C) Four working modes of TENG.

(D) The equivalent circuit model and electrical output equation of TENG. Reproduced with permission (Niu et al., 2014). Copyright©2014, Elsevier.

piezoelectric, or pyroelectric effect builds up the polarization field and become the foundation of nanogenerators.

Precisely, the *V*-*Q*-*x* relation of CS mode TENG can be expressed uniformly as

$$V = -\frac{Q}{S\varepsilon_0}(d_0 + x(t)) + \frac{\sigma x(t)}{\varepsilon_0} \quad \text{(Equation 2)}$$

In this equation, S is the surface area of electrodes and d_0 represents the effective thickness constant.

$$d_0 = \sum_{i=1}^{n} \frac{d_i}{\varepsilon_{ri}} \quad \text{(Equation 3)}$$

By means of the electrodynamic derivation, the intrinsic output performance of TENG can be expressed as

$$V_{OC} = \frac{\sigma x(t)}{\varepsilon_0} \quad \text{(Equation 4)}$$

$$Q_{SC} = \frac{S\sigma x(t)}{d_0 + x(t)} \quad \text{(Equation 5)}$$

$$C = \frac{\varepsilon_0 S}{d_0 + x(t)} \quad \text{(Equation 6)}$$

From Equation (6), the TENG has inherent capacitance properties of which the first-order equivalent circuit model is the series connection of a voltage source and a capacitor, as expressed in Figure 2D (Niu et al., 2014).

Considering that TENG converts mechanical energy into electrical signals directly, it can operate as a self-powered sensor without any power supply. The amplitude and frequency of generated electrical signals are highly related to the information of applied force consisting of pressure, motion, vibration, etc (Fan

et al., 2012b; Wang, 2013; Wang et al., 2015). In addition, as one of the most crucial parameters affecting the TENG output, the charge density on the friction layer is impressionable to many factors in the environment (Cheng et al., 2018; Kim, 2018). Therefore, TENG can also be used as a self-powered environment or chemical sensors to detect the humidity, light intensity, or concentrations of chemical components (Kim et al., 2018; Guo et al., 2014; Wang et al., 2020a). Moreover, it is more important to note that the material selection for fabricating TENG is quite ubiquitous that some functional materials such as ferroelectric, magnetic, or photosensitive materials can be adopted, which furtherly broadens the application range of TENG (Lee et al., 2016; Ren et al., 2017; Guo et al., 2020). Finally, the diverse structures of TENG should not be ignored because by appropriate structures design, the TENG is able to harvest more kinds of energy and use it for sensing (Park et al., 2015; Yu et al., 2017).

Prototypes

Motion and Force Sensors

Motion sensors are widely used in automatic production because of their wide variety and rapid development (Sasaki et al., 2017). The ability to sense the motion parameters such as displacement, speed, and acceleration direction is crucially important for the realization of automatic detection and automatic control (Jang et al., 2020; Fong and Chan, 2010). In 2018, Chen et al. developed a novel elastic-beam triboelectric nanogenerator (EB-TENG) by adopting an arc-stainless steel foil (arc-SSF) as electrode and friction layer simultaneously, as shown in Figure 3A (Chen et al., 2018a). A tailoring copper foil is pasted on the acrylic board and then PTFE as the friction layer is attached to it. One end of arc-SSF is gently fixed above the stratified structure in order to create the separation distance of TENG. A black rubber ring is employed to modulate the length of the device. Figure 3B displays the working mechanism of EB-TENG at different contact states under open-circuit conditions. The inherent capacitance of EB-TENG should be changed when pressing the SSF due to the affection of contact area (A) and separate distance (h); therefore, the open-circuit voltage (U) which is inversely proportional to the inherent capacitance changes with the pressing action. In order to better understand the working principles of EB-TENG, the authors carried out the finite element analysis (FEA) simulation about the potential distribution at initial and partially pressed state, as exhibited in Figure 3C. The results reveal that the potential of the contacting part of PTFE is lower than that of the separating part in both cases. Moreover, the potential difference between SSF and PTFE of the partially pressed state is smaller than the original state, which is caused by the charge coupling effect when the distance is close. As can be seen from Figures 3D and 3E, the voltage gradually increases with the increase of distance or force applied to the SSF, consistent with the simulation results. Further analysis shows that the sensitivity is about 30–900 V N^{-1} and 6 N mm^{-1}, which demonstrates the excellent feasibility as a multifunctional sensor of EB-TENG. In addition, the authors integrate the EB-TENG at the edge of a disk and mount on a rotating motor (Figure 3F). The EB-TENG undertake larger centrifugal forces when the motor is rotating at faster speeds, further achieving greater compression distortion. Intuitively, the voltage has a single correlation with revolving speed and acceleration (Figure 3G). Faster speed and larger acceleration are beneficial to the enhancement of voltage output. At the same time, the EB-TENG display advanced ability as a sensitive scale and vibration sensor, which encourages researches on the multifunctional self-powered sensor in the future.

Alternatively, Wu et al. introduced a translational-rotary TENG multifunctional sensor inspired by the movement statement of two magnets (Wu et al., 2019b). There is one magnetic disk (MD) fixed in an acrylic tube and another magnetic cylinder (MC) arranged at the periphery that can rotate around the tube, as schematically illustrated in Figure 3H. The TENG module is composed of a magnetic cylinder and PTFE friction layer with two interdigital electrodes attached to the surface of the acrylic tube. Figure 3I shows the optical photograph of entities. The mechanical analysis of the MS is illustrated in Figure 3J. Without the interference of external factors, the MC is subjected to gravity (G) of itself, the magnetic force (F_m), and supporting force (F_s) that is in a balanced state. Once there is an excitation (F_{ap} (a_{ap})), the MC will suffer the force along the opposite direction because of inertia and finally swing around the PTFE layer. If F_{ap} is strong enough, the MC is going to rotate on the friction layer periphery for several circles firstly and then into the swing stage. Therefore, the TENG generate electrical signals due to the relative movement between the MC and friction layer. Figures 3K and 3L describe the normalized voltage response of MS with various pairs of interdigital electrodes under different acceleration. When the acceleration is small, the voltages increase linearly with the increasing acceleration of all kinds of interdigital electrodes, which demonstrates excellent sensitivity. However, when the acceleration is above 4 m/s^2, the response should be measured by feature time, which is determined by the peak or valley from the V_{oc}. Simultaneously, the MS can detect the

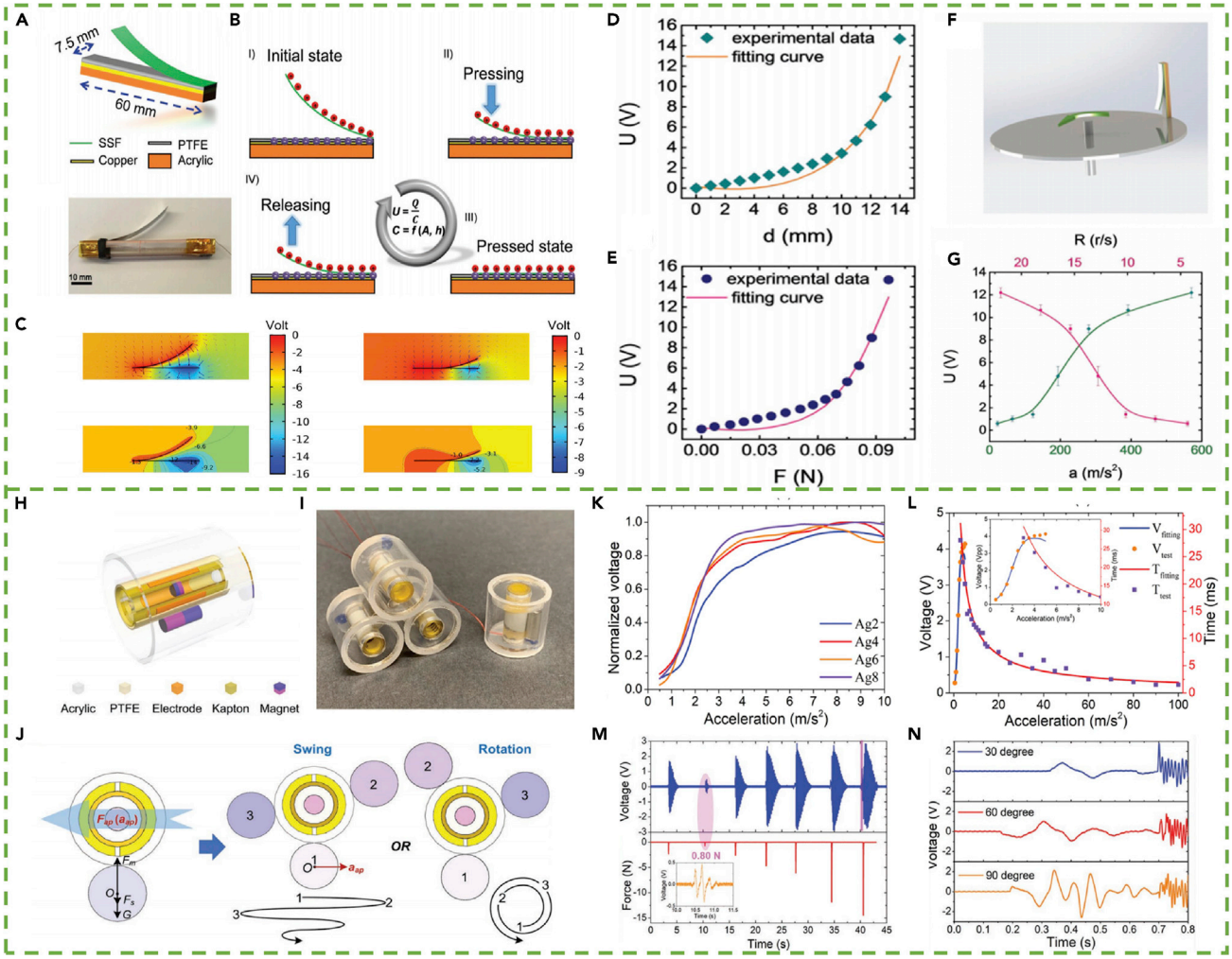

Figure 3. Motion and Force Sensor Based on TENG

(A)The schematic illustration (top) and the optical image (bottom) of the EB-TENG.

(B) The working mechanism of EB-TENG at the open-circuit condition.

(C–E) (C) The FEA simulation results of the potential distribution at initial (left) and partially pressed (right) state of the EB-TENG under open-circuit condition. The open-circuit voltage versus (D) separating distance (E) applied force.

(F) The schematic diagram for the acceleration sensor.

(G) The results of voltage with different revolving speed (*R*) and acceleration (a). Reproduced with permission (Chen et al., 2018a). Copyright©2018, Wiley-VCH.

(H and I) (H) Schematic illustration and (I) the optical photograph of entities of the translational-rotary TENG-based multifunctional sensor.

(J) The mechanical analysis illustration of the multifunctional sensor.

(K) Normalized voltages with various pairs of interdigital electrodes under different accelerations.

(L–N) (L) Peak to peak voltage values and feature time of the four pairs of interdigital electrode under different accelerations. Relationships of the voltage of the multifunctional sensor with different (M) hitting force and (N) swing angle. Reproduced with permission (Wu et al., 2019b). Copyright©2018, Wiley-VCH.

rotational parameters without coaxial installation due to the special structure characteristic of the translational-rotary magnetic mechanism. By placing the MS on the ball head of a golf club, it also is used as force and swing angle sensors, as shown in Figures 3M and 3N. More interestingly, the sensitivity of the MS can be dynamically adjusted by changing the distance of two magnet or the pairs of interdigital electrodes, which further broaden the scope of application.

Mechanical and Humidity Sensors

In general, the working environment of sensors in IoTs field is complex and changeable. Among them, the amount of water vapor or humidity in the air can affect human comfort and many industrial processes

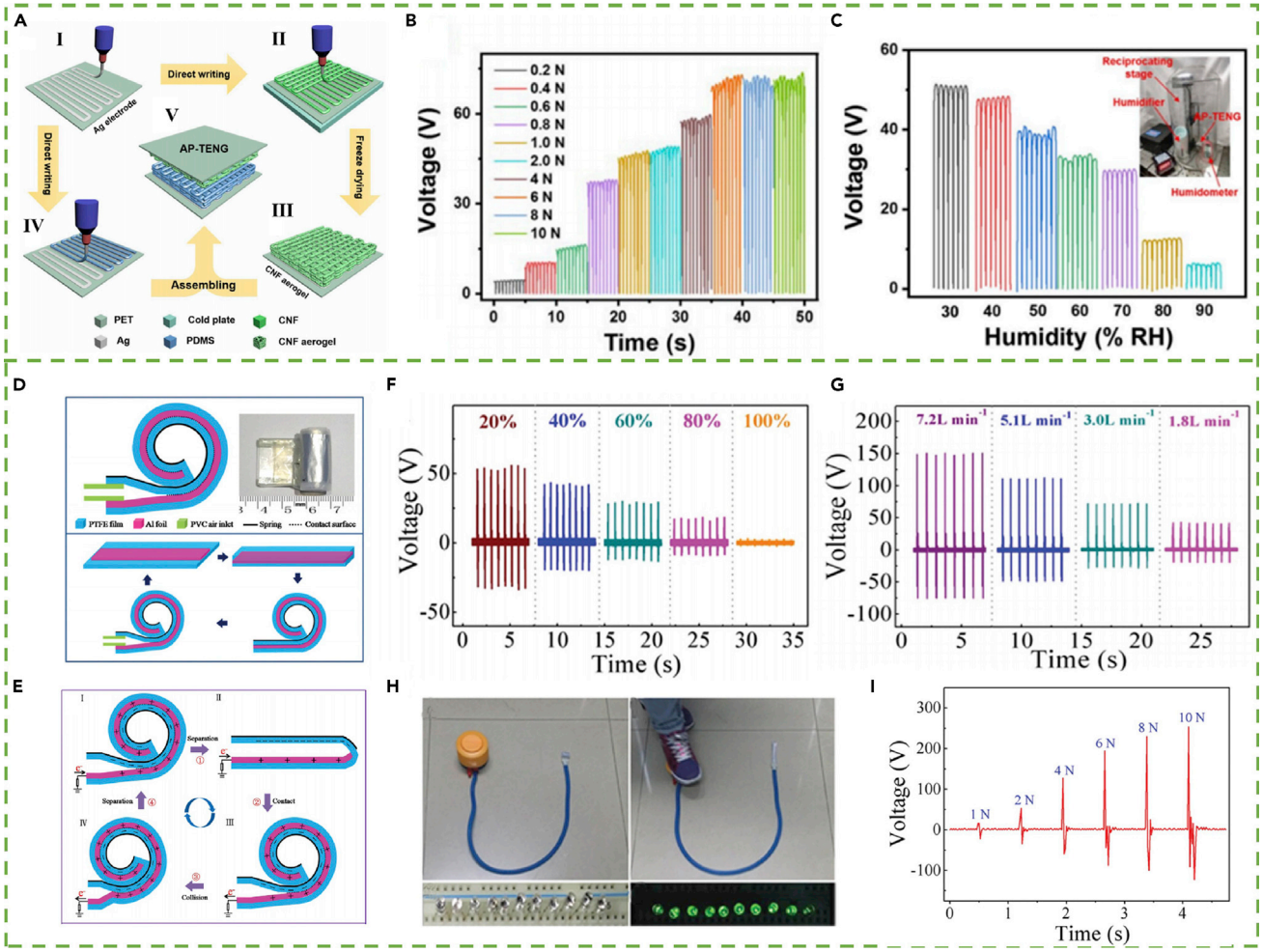

Figure 4. Mechanical and Humidity Sensor Based on TENG

(A) Schematic illustration of the AP-TENG fabrication process.

(B) The voltage output of AP-TENG at different forces.

(C) The relationship between voltage response and different humidity conditions. Reproduced with permission (Qian et al., 2019). Copyright©2019, Elsevier.

(D) Schematic diagram of device structure and fabrication process about the SR-TENG.

(E–G) (E) The working mechanism. The output voltage of SR-TENG with (F) different relative humidity and (G) air flow rate.

(H) The integrated motion monitoring system.

(I) The relationship of voltage and pressing force by foot. Reproduced with permission (Ma et al., 2015). Copyright©2015, Wiley-VCH.

(Henriques et al., 2017; Givoni et al., 2006). Therefore, it is important to develop multifunctional sensors that not only detect the mechanical factors but also monitor humidity levels dynamically and reliably. To this aim, Qian and co-authors fabricated excellent biocompatible cellulose-based TENG with 3D micro/nano hierarchically patterned structure by utilizing the all-printed method (Qian et al., 2019). Inevitably, micro/nanostructures are particularly beneficial to the enhancement of self-powered sensors based on the triboelectric effect. As illustrated in Figure 4A, the conductive Ag ink is printed firstly on the PET substrate with the desired pattern. Then, nano-porous cellulose nanofiber (CNF) aerogel is printed layer by layer with vertical alternation as the positive friction layer of TENG. In order to increase the triboelectric and roughness, the CNF layer is treated with freeze-drying and post-annealing process. Meanwhile, the PDMS ink is squeezed out from the nozzle onto the Ag pattern, forming the negative friction layer. In the end, the CNF and PDMS layer is assembled into a sandwich structure, forming the multifunctional sensor device. It is found in Figure 4B that the output voltages increase gradually along with the rising press force that ranges from 0.2 to 10 N, which shows outstanding potential for mechanical sensing application. In order to gauge the sensitivity performance as a humidity sensor, the voltage output is tested under a range of relative humidity conditions. As exhibited in Figure 4C, with the relative humidity

increasing from 30% to 90% in a closed system, the open-circuit voltage reduced almost linearly because of the unique material selection and structure designation. In the real application scenario as a single-channel multifunctional sensor, there should be a standard reference value of voltage comparing with the test voltage value to determine the force or humidity to obtain the corresponding sensor data. This function is usually implemented by a back-end processing circuit. More importantly, this work provides a novel strategy to fabricate a multifunctional sensor that will be useful for the electronic device field.

Self-recovering characteristic is deeply significant to the sensors, which need a long time and continuous working (Zhong et al., 2016; Zhao et al., 2019). Ma et al. designed a special self-recovering triboelectric nanogenerator (SR-TENG) with a quickly relative movement between two friction layers (Ma et al., 2015). As illustrated in Figure 4D, the SR-TENG contains a piece of Al foil as both electrode and friction layer are sandwiched between the PTEF bag. An annular spring has adhered to one side of PTFE, and a PVC air inlet is fixed at the end of the device for the air flowing from it. When air is injected into the PTFE bag, the spring deforms from the coil into flat due to internal gas expansion, further causing the friction layers' transformation from contact state to separation state (Figure 4E). In this process, the electrons flow back and forth between the ground and the electrode; in other words, the TENG is triggered and generates electrical signals in an air injection and outflow cycle. Similar to previous reports, the SR-TENG is sensitive to environmental relative humidity, as the results show in Figure 4F. The increase in relative humidity resulted in a significant decrease in the open-circuit voltage at a constant airflow rate. This tendency can be explained by the triboelectric charges screen effect caused by the water molecules absorbing onto the friction layers to form a water layer in a humid environment. Moreover, in consideration of the fact that higher airflow rate leads to faster separation and contact movement between PTFE and Al electrode, the output voltage of SR-TENG is supposed to generator a larger value at a higher airflow rate and obtain higher sensitivity at lower humidity, just as Figure 4G shows. In addition, the authors integrate the SR-TENG with an air pump and a bunch of LED lights that connect in series to demonstrate its capacity as a motion monitor (Figure 4H). When humans put a foot on the air pimp, the SR-TENG swell due to air injection; therefore, the electrical signals come into being and the LEDs are lighted up. Particularly, as displayed in Figure 4I, higher open-circuit voltage is going to generator along with heavier pressing force, which revealed the feasibility of SR-TENG in motion monitoring.

Biological and Chemical Sensors

Water is the source of human life and the foundation of all living things. But it is easy to be contaminated as a polar solvent for dissolving many ionic components (Eric et al., 2020). Even worse, some harmful microorganisms such as viruses or bacteria can live in water, which is a threat to human health (Li, 2013; Goncharuk et al., 2018). Consequently, it is urgent and eager to invent self-powered biomedical and chemical sensors with short detection time and low cost.

Chen and coauthors introduced a biological and chemical micro liquid detection system based on a capillary-tube triboelectric nanogenerator (CT-TENG) (Chen et al., 2018b). The structure and fabrication process of the device is schematically displayed in Figure 5A. Two mutually dislocated helical electrodes wrap around the outside surface of the PTFE capillary tube. In the meantime, a silicon rubber with heat shrinkable property is adopted as an encapsulation layer. The working process of the CT-TENG mainly divides into four steps after connecting with a syringe, as shown in Figure 5B. Once injecting micro liquid into the PTFE hollow tube, the contact electrification happened due to the relative movement of the two friction layers, as shown in the side and front views (Figures 5C and 5D). To demonstrated the micro liquid chemical sensing ability of CT-TENG, the authors tested ten different ionic standard solutions, including Na^+, Mg^{2+}, Zn^{2+}, Cu^{2+}, Sn^{2+}, Al^{3+}, NH_4^+, Cl^-, NO_3^-, and SO_4^{2-}, at the constant volume, which is diluted by deionized water. The electrical output results of voltage are intuitively displayed in Figure 5E. It is important to note that all the electrical output of CT-TENG is highly correlated with the electrical conductivities (κ) of various ionic standard solutions (Figure 5F). On the basis of these curves, the CT-TENG owns great potential applications as self-powered sensors for micro liquid detection according to κ contribution. Moreover, as shown in Figure 5G, the electrical output of CT-TENG goes gradually down as time goes on when injecting the barreled water into it. This phenomenon can be explained by the accumulation of the total dissolved solids and κ of barreled water with the extension of storage time. These solids in water are negatively charged, which reduces the output of TENG. Figure 5H reveals the positive linear correlation relationship of signals of CT-TENG and electrical conductivities of KCl solution with different concentrations. According

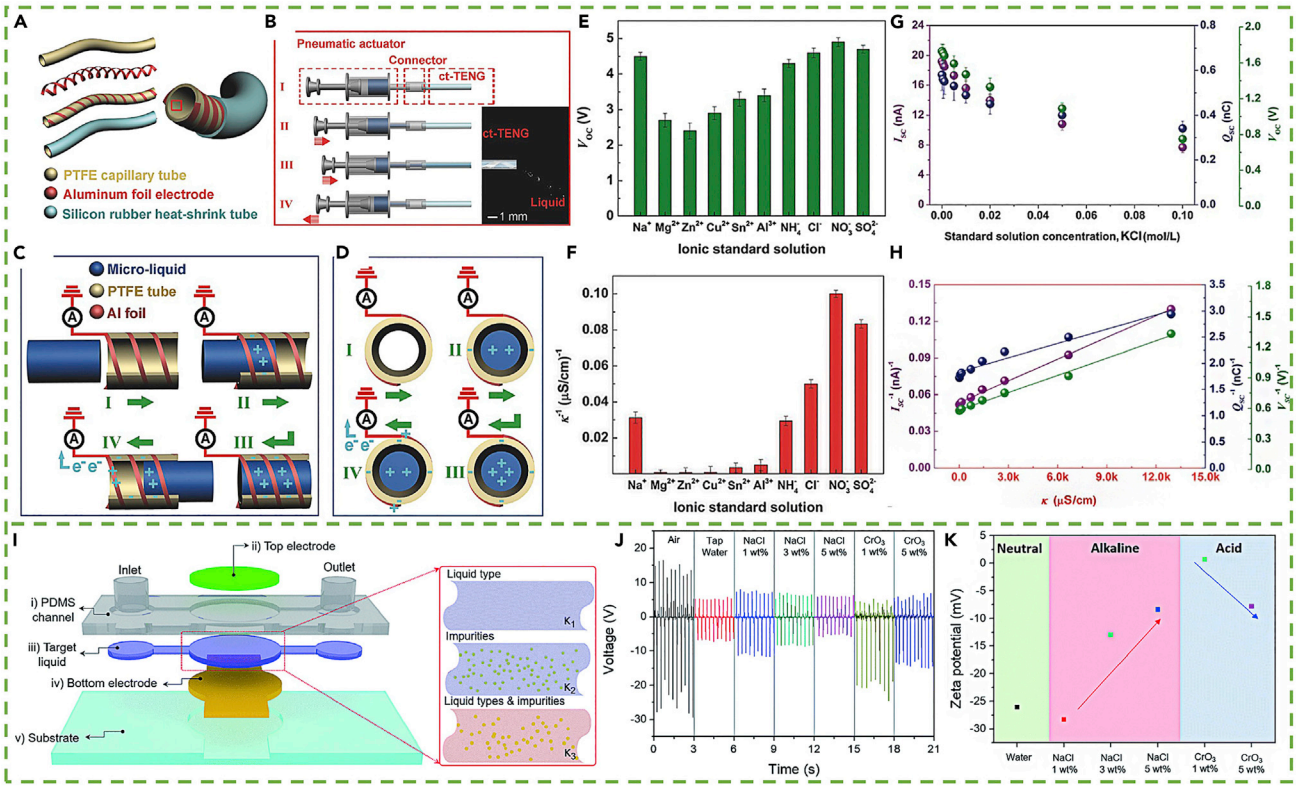

Figure 5. Biomedical and Chemical Sensors Based on TENG

(A) Schematic illustration of the CT-TENG structure.

(B–D) (B) The working process. The working mechanism diagram of CT-TENG in (C) side and (D) front views.

(E and F) (E) The open-circuit voltage and (F) electrical conductivity with different ionic standard solutions.

(G) Electrical output of the CT-TENG at different drinking time.

(H) The relationship between the electrical conductivity and output signals of CT-TENG. Reproduced with permission (Chen et al., 2018b). Copyright©2018, Wiley-VCH.

(I) The 3D diagram of the microfluidic system.

(J) The voltage output with air and solutions with different concentrations and solvent.

(K) The zeta potential of various liquids. Reproduced with permission (Kim et al., 2018). Copyright©2018, Royal Society of Chemistry.

to the results, the CT-TENG can directly monitor κ with little micro liquid with the significant advantage of highly flexible, microliter sampling, and low cost.

Moreover, Kim et al. developed a simple self-powered microfluidic system for fast and real-time liquid sensing, of which signals originate from the electrical behavior of different liquids in the electric field generated by the triboelectrification effect (Kim et al., 2018). As illustrated in Figure 5I, the sensing system mainly contains four modules: substrate, micro-structured PDMS channel, top and bottom electrodes. The PDMS channel is fabricated by spin-coating the precursors onto a patterned template which is manufactured by lithography method. Top and bottom electrodes are deposited on the glass side that acts as the substrate. In the final step, the PDMS channel and electrodes are bonded together via the oxygen plasma treatment. Once the tap water is injected into the channel, the voltage signals are significantly reduced compared with the air filling device, as displayed in Figure 5J. The reason is probably that the electric field is going to decrease considering that all the liquids are polar components and the ions will couple with the transferred electrons on the PDMS surface to form the electric double layers. Accurately, the authors adopt the NaCl and CrO_3 aqueous solutions with different concentrations besides air and tap water. It can be seen that with the increasing concentration, the voltages weaken almost proportionally. These results support the conclusion that free ions could interrupt the electric field intensity. To analyze the relationship between the output and the characteristic parameters of the liquid in detail, the zeta potential of different liquids is tested. As shown in Figure 5K, there is a high negative correlation between the two factors, which

demonstrate the excellent ability of the microfluidic system to sense the liquid types and impurities in the biomedical and chemical industries.

Other Sensors Based on TENG

In recent years, with the continuous development of electronic technology and automation, pneumatic flow and liquid level measurement have become increasingly prominent. The production of daily chemical products, marine engineering construction, and early warning of marine disasters cannot be separated from the monitoring of liquid level (Shao et al., 2020; Fu et al., 2020). For promoting the application of TENG in SPMS, Wang et al. designed a magnetic flap-type multifunctional sensor system based on the triboelectric effect, which can be used to detect pneumatic flow and liquid level (Wang et al., 2020b). The main components of the sensor system include a magnetic float that can be moved up and down by applying force and therefore create a moving magnetic field, a magnetic flap of which half of the surface is covered by copper electrodes with half-cylinder shape that can rotate 180° by the direction of the external magnetic field, as exhibited in Figure 6A. Copper plates are adopted as electrodes, and assembled acrylic boards act as the support frame. The working principle of the multifunctional sensor system is graphically shown in Figure 6B. The theorem of impulse, connector, and magnetic coupling principles are the theoretical foundation for realization. In the original state, the overlapping copper electrode and PTFE are electrically neutralized. Once air flows in or rises above the liquid level of the conical cavity, the magnetic float moves upward and rotates the adjacent magnetic flap until the copper electrodes flip over to face directly to PTFE. The positive charges are going to be induced on the half-cylinder copper electrodes, therefore changing the charge potential of the system and generating electrical signals. To assess the ability of the system for flow rate detection, the open-circuit voltage is measured under a series of flow rates from 10 to 200 L/min. The results are displayed in Figure 6C that the peak value of voltage promotes approximately linearly as the flow rate increases. By comparing with a commercial flow switch, the authors demonstrate the excellent feasibility of the system to detect the change of flow rates under regular motion (Figure 6D) and irregular motion (Figure 6E) regardless of flow direction. The minimum detectable flow rate is about 2 L/min, and the flow resolution in the forward and reverse directions is 7.85 and 7.47 L/min, respectively. In addition, the system can sensor different liquid levels according to the theory analysis. As shown in Figure 6F, the output voltages gradually increase with the rising of liquid heights from 30 mm to 130 mm and keep almost constant at the fixed flow rates condition. Similarly, they designed a liquid-level height detection platform to evaluate the performance of the device. The liquid height is dynamically recorded through the software, and the corresponding voltage is measured synergistically. As exhibited in Figures 6G and 6H, voltage responses are timely and accurate no matter the liquid level rises or falls. Thus, it is absolutely meaning for rainfall detection of this work.

As the body's largest organ, human skin can block most bacteria and dirt outside the body and also ensure the body to sense the pressure and temperature (Herman and Herman, 2019). For the purpose of intimating the function of skin, the electronic skin is developed and attracts tremendous attention from scientists and industrialists (Zhu et al., 2020a; Oh and Bao, 2019; Ma et al., 2019a). For example, Rao et al. developed tactile e-skins (TES) based on the TENG with a single electrode that can detect and distinguish the temperature and pressure simultaneously but the two stimuli do not interfere with each other (Rao et al., 2020). As illustrated in Figure 6I, the special design of the TES relies on its thermo-resistive electrode that is formed by dispersing the $BiTiO_3$ and rGO powder into the PVDF solution and dried on the PDMS surface. In order to enhance the pressure detection sensitivity, the pyramidal microstructures are fabricated on another PDMS surface by the template transfer method. It can be seen that the resistance of the electrode keeps linearly increasing with the reciprocal of the temperature no matter whether to bend the device (Figures 6J and 6K). The sensing range of temperature is 25–100°C, and the highest temperature coefficient of resistance (TCR) is 1.15%/K at 25°C, which well satisfies the wearable electronics. The electrical output of the TES partly depends on the surface triboelectric charges that are positively proportional to the contact area of two friction layers. In case of applying different pressure on the device, the microstructures undergo squeeze to varying degrees, which causes the changed contact area and hence different amplitudes output is going to produce. This assumption is experimentally demonstrated in Figure 6L; the relationship between the open-circuit voltage of the TES and pressure keeps almost linear in two sections that are consistent with previous reports. The sensitivity is 5.07 mV/Pa in the smaller pressure range and 1.89 mV/Pa in the larger pressure range. In order to detect and distinguish the temperature and pressure at the same time, they construct a TES array with 5 × 5 pixels and connect to the Keithley and multimeter, respectively, as schematically illustrated in Figure 6M. When placing a square heater above the TES array (Figure 6N), the temperature and pressure distribution map are straightforwardly displayed in Figures 6O and 6P. The non-interference can be explained by the resistance change range of the electrode (below 40 MΩ), which is

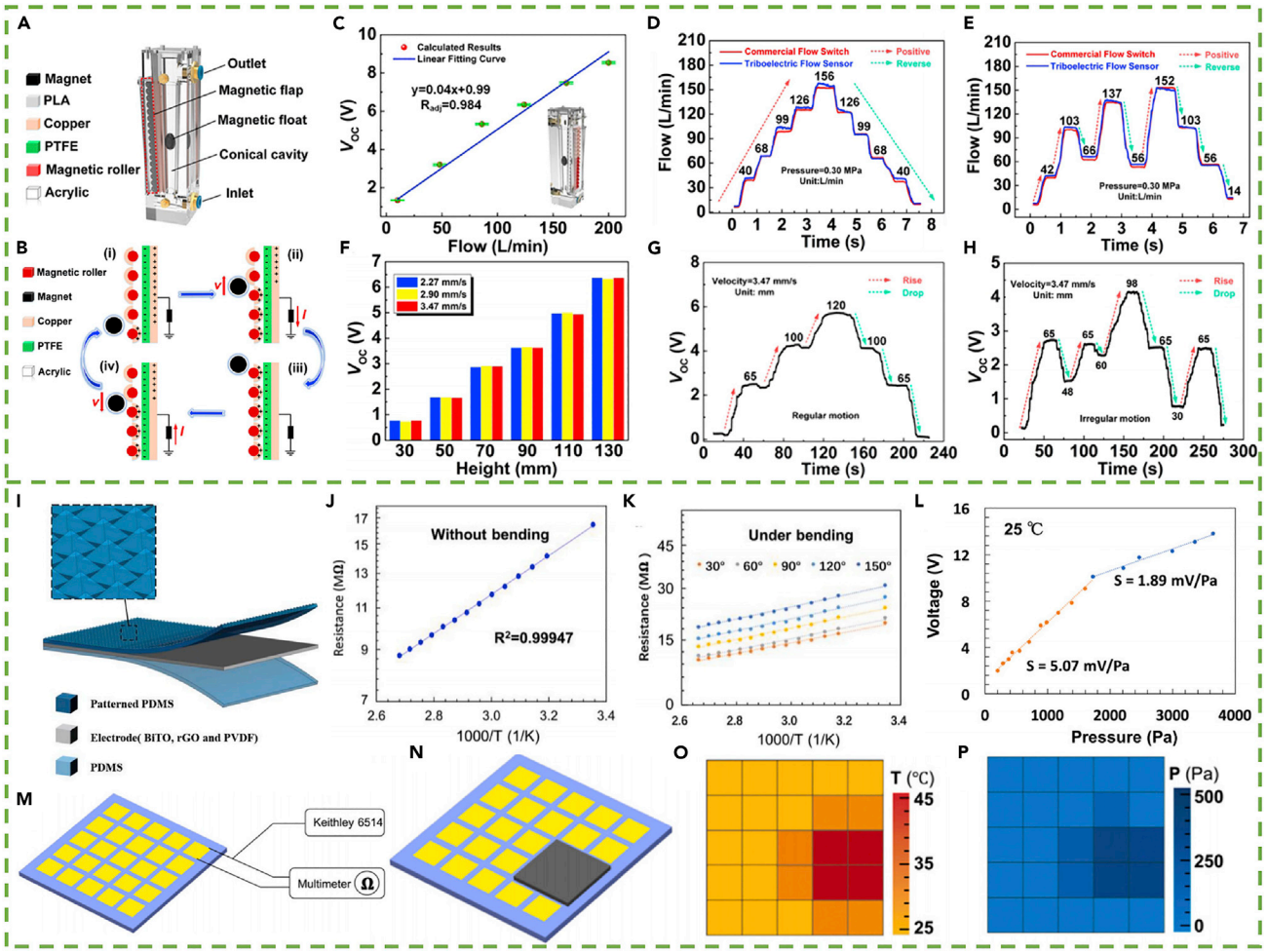

Figure 6. Other Sensors Based on TENG

(A) Schematic illustration of the magnetic flap-type multifunctional sensor system.

(B) The working mechanism.

(C–E) (C) The open-circuit voltage with different flow rates. The dynamic detection of flow rates under regular motion (D) and irregular motion (E).

(F–H) (F) The voltage response under different liquid level heights. The dynamic detection of liquid level heights under regular motion (G) and irregular motion (H). Reproduced with permission (Wang et al., 2020b). Copyright©2018, American Chemical Society.

(I–K) (I) The 3D diagram of the tactile e-skin. The relationship of resistance and the reciprocal of the temperature under (J) without bending and (K) different bending states.

(L) The voltage response under various pressure.

(M) The tactile e-skin array with an array with 5 × 5 pixels.

(N) The square heater above the array.

(O and P) (O) The temperature and (P) pressure distribution map of Figure 6N. Reproduced with permission (Rao et al., 2020). Copyright©2020, Elsevier.

absolutely small compared with the intrinsic resistance of TENG (around 800 MΩ). This work offers new possibilities for the application of electronic skin, medical care, or prosthetics fields.

MULTIFUNCTIONAL SELF-POWERED SENSORS BASED ON BINARY-HYBRIDIZED NANOGENERATORS

Principles

Piezoelectric Nanogenerators

PENG is the first proposed nanogenerator that relies on the piezoelectric effect of materials such as regularly arranged ZnO nanowires (Nour et al., 2014), lead zirconate titanate (PZT) (Cui et al., 2016), $BaTiO_3$ (BTO) (Park et al., 2010), poly(vinylidene fluoride) (PVDF) (Khalifa et al., 2019), or other 2D materials

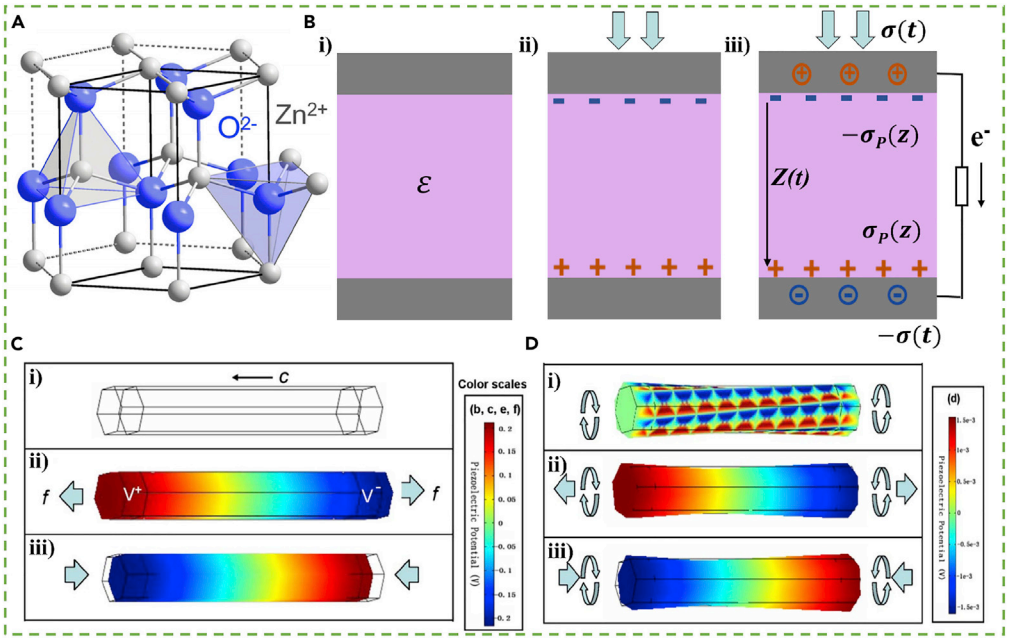

Figure 7. The Multifunctional Self-Powered Sensing Mechanism of PENG

(A) Hexagon wurtzite crystal structure of ZnO.

(B) Schematic illustration of PENG principle under pressing. Reproduced with permission (Wang, 2017). Copyright©2017, Elsevier.

(C) The simulation results of the piezoelectric effect under (i) original state, (ii) stretching, and (iii) compressing.

(D) The simulation results of piezoelectric effect under (i) twisting, (ii) twisting and stretching, and (iii) twisting and compressing. Reproduced with permission (Gao et al., 2009). Copyright©2009, American Institute of Physics.

(Peng et al., 2018; Maity et al., 2017; Duggen et al., 2018). PENGs can convert mechanical energy such as bending or compressing into electricity because the piezopotential is going to be generated once the central symmetry of piezoelectric materials' crystal structure is broken (Gao et al., 2009). For instance, the crystal structure of ZnO is hexagon wurtzite with the Zn^{2+} and O^{2-} stacking layer by layer along with the *c*-axis, as displayed in Figure 7A (Zhang et al., 2003). Due to the symmetrical distribution of anions and cations, the charge center is completely coincident in the absence of external interference (Figure 7B-i). However, once an external force is applied, the material will inevitably deform, and the center of positive and negative charges will deviate from the original position. Therefore, an electric dipole is formed and leads to the generation of piezopotential (Figure 7B-ii). And peculiarly, the piezopotential difference intends to be equilibrium by free electron flowing if an external load is connected to the top and bottom electrodes forming a complete loop, as can be seen in Figure 7B-iii. In other words, the electricity of PENGs is generated by applying mechanical stimuli (Kim et al., 2019).

It is more important to note that the theoretical source of PENGs is also the second component of Maxwell's displacement current (Wang, 2017). With the increasing of applied force, the polarization charge density ($\sigma_P(z)$) increases accordingly. The density of charge on the electrodes is marked as $\sigma(z)$, which is a function of the thickness of the piezoelectric material. For the condition of Figure 7B-i without an external electrical field, the polarization direction is following *z* axis, and the displacement field equals the polarization vector in the media, $D_z = P_z = \sigma_P(z)$; therefore, the displacement current is

$$J_{D_z} = \frac{\partial P_z}{\partial t} = \frac{\partial \sigma_P(z)}{\partial t} \quad \text{(Equation 7)}$$

The Equation (7) reveals that the output current of the PENGs is directly proportional to the changing rate of polarization charges on the surfaces. Considering the open-circuit voltage is

$$V_{OC} = z\sigma_P(z)/\varepsilon \quad \text{(Equation 8)}$$

If an external load *R* is connected, the current output equation will be

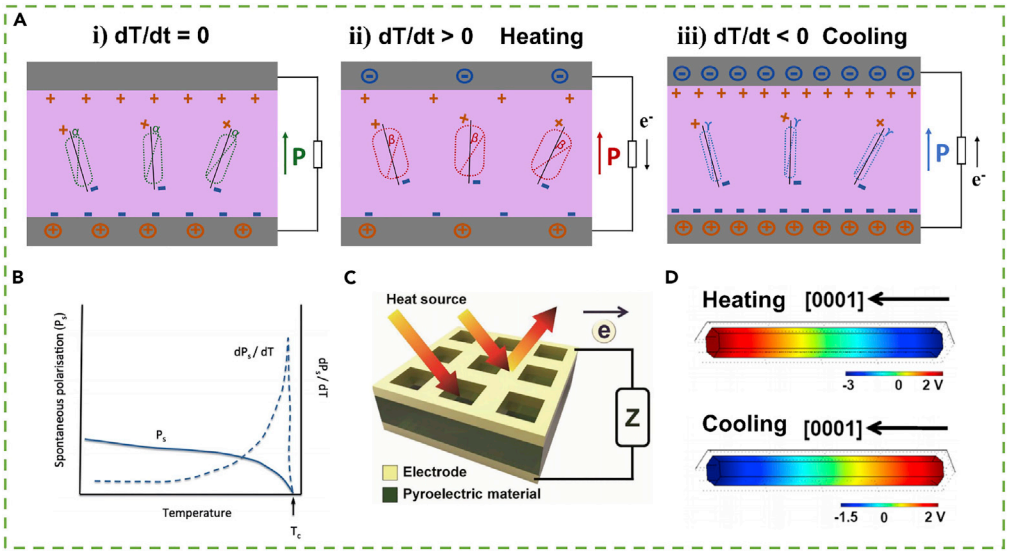

Figure 8. Principles of PyENG

(A) Schematic illustration of the mechanism of PyENG under (i) fixed temperature, (ii) heating, and (iii) cooling conditions. Reproduced with permission (Wang et al., 2012). Copyright©2012, Elsevier.

(B) The quantitative relation between P_s and temperature.

(C) The typical sandwich structure of PyENG. Reproduced with permission (Ryu and Kim, 2019). Copyright©2019, Wiley-VCH.

(D) The simulated potential distribution in a single ZnO nanowire when heating and cooling states. Reproduced with permission (Yang et al., 2012). Copyright©2012, American Chemical Society.

$$RA\frac{d\sigma}{dt} = z[\sigma_P(z) - \sigma(t)]/\varepsilon \qquad \text{(Equation 9)}$$

In Equation (9), A stands for the area of electrodes. In terms of the slow rate of applied strain in our daily life, the thickness z is almost the function of time t. Hence, the PENG is adopted as a pressure sensor solely or in combination with other sensors. In addition, as the simulation results of piezoelectric potential distribution, the PENGs detects not only stretching or compressing force (Figure 7C) but also a twisting force or multiple forces applied simultaneously (Figure 7D), which further expands the application range of PENGs in the sensing field.

Pyroelectric Nanogenerators

Thermal energy is another widespread form of energy in the surrounding environment and our daily life but most of it is wasted (Roth and Brodrick, 2009; Alva et al., 2017). Previously, people tried to harvest thermal energy by the Seebeck effect (Zianni, 2014; Nakatani et al., 2009). The effect relates to a thermoelectric phenomenon in which the voltage difference is generated by the temperature gradient between two different electrical conductors or semiconductors. However, if the external temperature does not have a gradient but changes with time, the Seebeck effect becomes ineffective, and the pyroelectric effect is used to collect heat energy.

Similar to the piezoelectric effect, the pyroelectric effect is a natural physical effect of crystals that the polarization intensity changes with the temperature instead of mechanical contact, as shown in Figure 8A (Wang et al., 2012). The typical pyroelectric materials (PyEM) spontaneously polarize at internal (P_s) even without external electric field or temperature change (dT), as presented in Figure 8A-i. Although wiggling atoms break the alignment balance of the internal dipole, the spontaneously polarized electric dipoles cannot be displayed because P_s and wiggling angle (WA) α are always constant in the absence of temperature change ($dT/dt = 0$). When heating the material ($dT/dt > 0$), higher temperatures increase the vibration of atoms, and larger WA is obtained ($\beta > \alpha$). After that, the P_s intension decreases, and furtherly the induced charges on the PyEM surface (Q) reduce. In consequence, the free electrons are going to flow through the external circuit with the generated current intensity (i) equals to

$$i = \frac{dQ}{dt} = pA\frac{dT}{dt} \qquad \text{(Equation 10)}$$

where p is the pyroelectric coefficient, A is the surface area of PyEM, and t is time. On the contrary, if the temperature decreases ($dT/dt < 0$), WA becomes smaller ($\gamma<\alpha$) on account of the reduced vibration motion of wiggling atoms, leading to the increased polarization. Moreover, the induced surface charges increase and free electrons flow in the reverse direction. The quantitative relation between P_s and temperature is shown in Figure 8B (Ryu and Kim, 2019). P_s decrease with the temperature rises, whereas it rapidly becomes zero if the Curie temperature (T_C) arrives. Through the above analysis, PyENG can be primitively fabricated by sandwiching the PyEM into two pieces of electrodes, as illustrated in Figure 8C. In addition, Figure 8D expresses the simulated potential distribution in a single ZnO nanowire when heating and cooling states (Yang et al., 2012).

Prototypes

Triboelectric/Piezoelectric Effect

In addition to mimicking the sensing function of human skin, the electronic skin is often used as a wearable device for human physiological signals health monitoring, such as pulse, heartbeat, or breath detection (Qi et al., 2017; Guo et al., 2018). Zhu et al. developed a wearable all-in-one hybrid electronic skin (HES) for multifunctional sensing depending on the combination of triboelectric and piezoelectric effects (Zhu et al., 2020b). As displayed in Figure 9A, the HES mainly contains a triboelectric layer, a piezoelectric layer, several pieces of conductive fabric as electrodes, and a PDMS substrate. The porous PDMS layer is formed by the natural lotus leaf as the template. Semicrystalline PVDF powder is dissolved in the MWCNTs suspension to form a homogeneous solution and the MWCNT-doped PVDF membrane is fabricated via electrospinning method, which obtains enhanced piezoelectric properties due to the addition of MWCNTs motive the orientation of PVDF molecular chains. The conductive fabric ensures the flexibility of the HES and therefore can be attached to the human body comfortably (Figure 9B). When an object touches the HES, as shown in Figure 9C, a whole cycle can be divided into four steps: contact, compressive deformation, rebound recovery, and separation process. During the initial and final process, the electric signals are generated on account of the triboelectric effect, and the piezoelectric effect is the foundation in the middle process. As described in Figure 9D, the HES responses are approximately linear in two different pressure ranges. The sensitivity reaches to 54.37 mV/kPa at a lower pressure region (<80 kPa), whereas it decreases to 9.8 mV/kPa when the pressure increases. By attaching the HES to the artery in the neck of a volunteer (Figure 9E), there will be evident signals when the man speaks as the vocal cord vibrates, as exhibited in Figure 9F. The frequency is mostly distributed in a range of 50–500 Hz, which demonstrated that the HES can be used as vocal rehabilitation training or voice recognition. More importantly, the sensitivity is outstanding that a typical pulse signal can also be detected with three distinct peaks, which is a significant reference to evaluate a person's health (Figure 9G). In order to obtain the ability to recognize the shape of an object, a 4 × 4 sensor array is assembled, as shown in Figure 9H. By placing the plastic blocks shaped as letters "S", "K", "I", and "N", different planar voltage distribution maps can be drawn according to the output of the sensor array and distinguish the shape accurately (Figures 9I–9L).

Similarly, Yu et al. reported that a highly skin-conformal tactile sensor (STS) relies on a couple of triboelectric and piezoelectric effects (Yu et al., 2019). As a widely used polarized piezoelectric material, the lead-zirconate-titanate (PZT) nanofibers are chosen to mix with the PDMS base and solidified to form the film. The unpolarized film acts as the tribo-friction layer while the deformation of polarized film generates piezoelectric signals, as illustrated in Figure 9M. The STS is conformal and comfortable when contacting with irregular human skin and can withstand complex deformations. To evaluate the sensing performance, the voltage response under different force is measured. As exhibited in Figure 9N, the tendency is consistent with pressure sensors of previous reports that achieve a higher sensitivity at a small pressure region and a depressed value at a larger pressure region. The wrist pulse is a dominant parameter of heart rate and provides much important information for cardiovascular diseases. Hence, the pulse waveform is measured by the STS and the result can be seen from Figure 9O. The percussion wave (P-wave), tidal wave (T-wave), and diastolic wave (D-wave) are clearly detected and the amplitude or velocity can be further analyzed to evaluate the health condition. Because of the simple structure of STS, it can be easily integrated into an array with the shared nonpolarized film and independent piezoelectric parts, which is marked as "1" to "9." The trajectory of the finger sliding can be recorded from the output of each pixel, as displayed in Figure 9P. In addition, the STS can monitor the human postures comprehensively once attaching it to the heel. As can be seen in Figure 9Q, various actions such as walking, running, tiptoe walking, or jumping are detected by the STS, which demonstrated the potential application in wearable electronics.

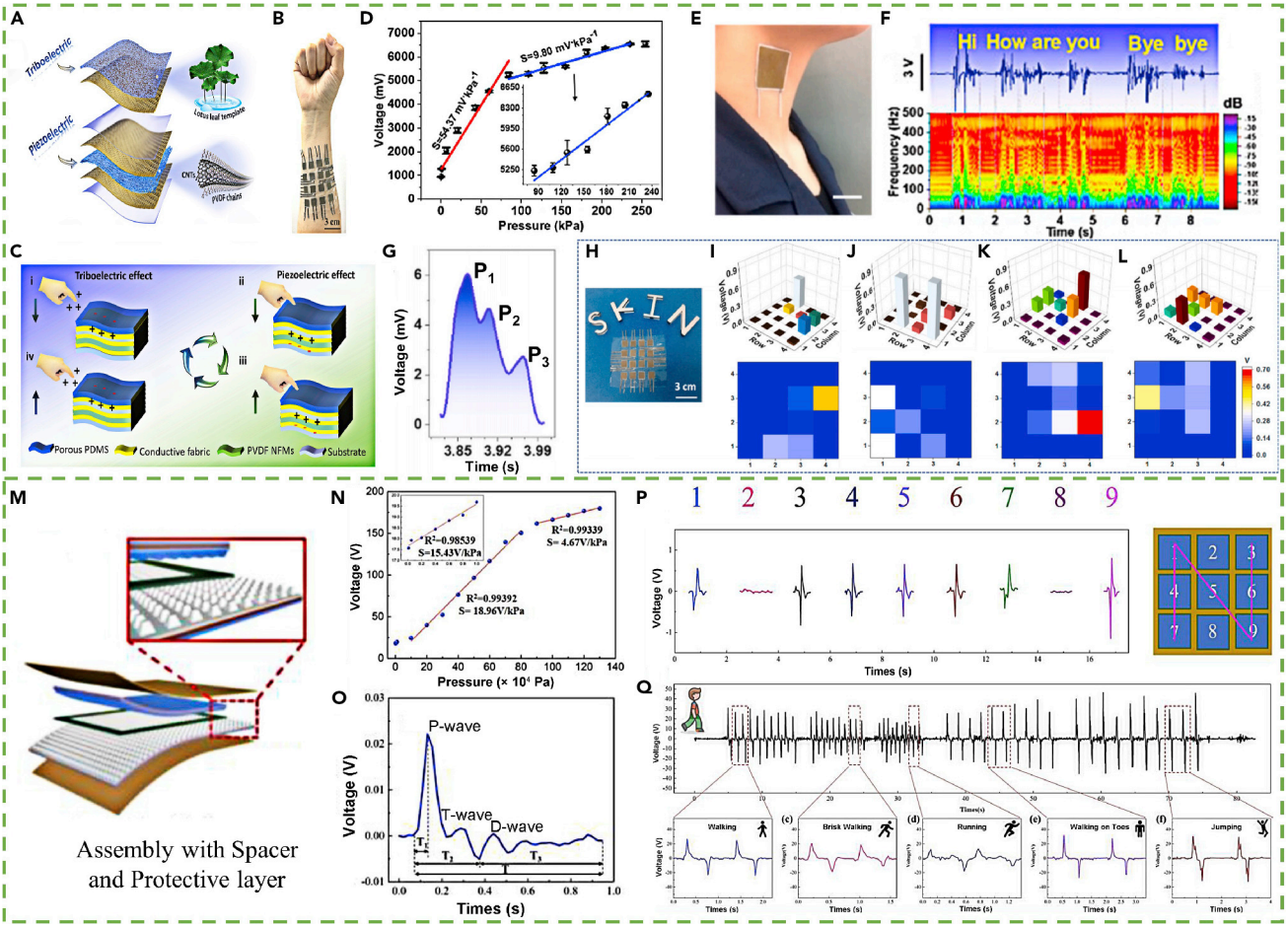

Figure 9. Multifunctional Sensors Based on the Triboelectric and Piezoelectric Effect

(A) Schematic illustration of HES.

(B) Optical picture of the HES attached to the human arm.

(C) The working mechanism.

(D) The sensitivity of HES as a pressure sensor.

(E) Photography of the HES attached to the artery in the neck.

(F) The voltage and frequency under different vocal cord vibrate.

(G) A pulse waveform.

(H) The 4 × 4 sensor array.

(I–L) The voltage distribution maps of plastic blocks shaped as letters "S", "K", "I", and "N". Reproduced with permission (Zhu et al., 2020b). Copyright©2020, Elsevier.

(M) Schematic illustration of STS.

(N) The performance of pressure sensor.

(O) The pulse waveform.

(P) The output of sensor array and trajectory of the finger sliding.

(Q) The voltage responses under different actions. Reproduced with permission (Yu et al., 2019). Copyright©2019, Elsevier.

Triboelectric/Pyroelectric Effect

Nowadays, the health of unborn babies is a considerable issue faced by new parents. However, electronic products have become an indispensable part of daily life, such as phones, computers, or tablet PCs, which will produce radiation pollution all the time (Psenakova and Hudecova, 2009; Ankerhold et al., 2009). In order to protect the pregnant from electromagnetic radiation injury and monitor the health conditions, Zhang et al. designed an electromagnetic shielding hybrid nanogenerator (ES-HNG) with a large-sized stretchable TENG as the substrate and several pyroelectric-piezoelectric nanogenerators (PPENGs) that uniformly dispersed on it to form an island structure, as illustrated in Figure 10A (Zhang et al., 2018). A piece of anti-electromagnetic radiation fabric is

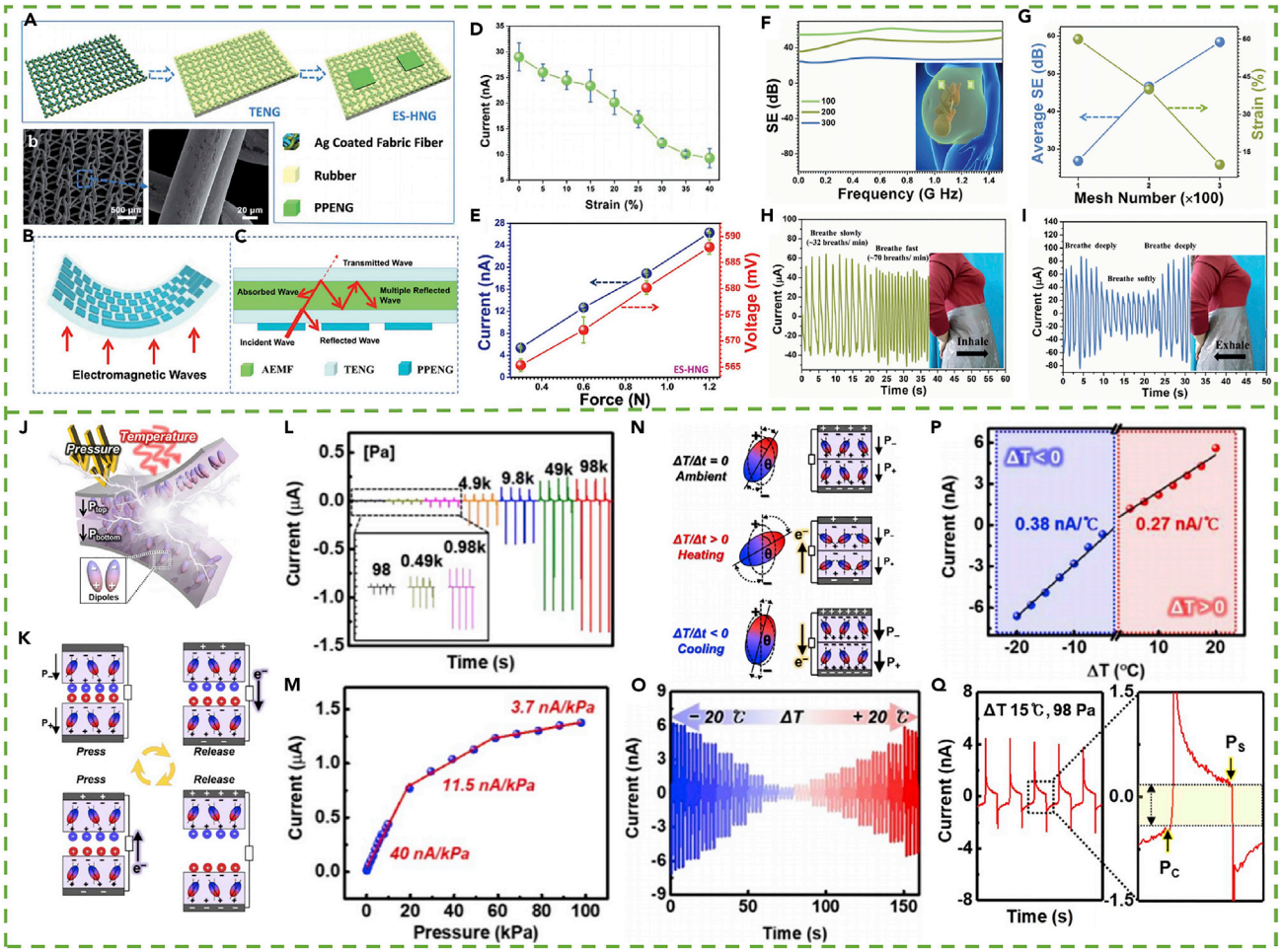

Figure 10. Multifunctional Sensors Based on Triboelectric and Pyroelectric Effects

(A) The fabrication process of ES-HNG.

(B) The schematic of the ES-HNG based keyboard.

(C) The principle of electromagnetic wave shielding.

(D) The current under different tune.

(E) The electrical performance with different force.

(F) The SE of large area ES-HNGs under different meshes of AEMFs.

(G–I) (G) The average SE and strain using different meshes. The current response under different (H) breathes rate and (I) breathe strength. Reproduced with permission (Zhang et al., 2018). Copyright©2018, Wiley-VCH.

(J) The schematic diagram of PTMS.

(K) The triboelectric working mechanism.

(L) The real-time current response under various pressure.

(M) The sensitivity as a pressure sensor.

(N) The pyroelectric working mechanism.

(O) The pyroelectric current under different temperatures.

(P) The linear relationship between current and temperature gradient.

(Q) The current signal and enlarged peak when applied pressure and heating temperature, simultaneously. Reproduced with permission (Shin et al., 2020). Copyright©2020, Elsevier.

adopted as the conductive electrode (Figure 10B). The electromagnetic wave will go through multiple reflected, absorbed process and finally decrease dramatically compared with the initial value (Figure 10C). Consequently, the ES-HNG is able to fabricate as a keyboard and protect the user from electromagnetic fields emitted from the external environment effectively, as shown in Figure 10B. The electrical output of the ES-HNG decreases almost linearly with the increase of elongation from 0% to 40% for the reason that the charge density decreases and resistance increases synchronously with the elongation (Figure 10D). Moreover, the relationship between current

and voltage performances and force is investigated. As displayed in Figure 10E, the two factors are both linearly increased with the applied force ranging from 0.3 to 1.2 N, which verifies the feasibility as a pressure sensor. Considering the damage of electromagnetic radiation to the fetus inside the pregnant woman, the authors developed a large area of ES-HNG as a self-powered protection and monitor system. In order to obtain optimal protection performance, three different mesh number fabrics are adopted, respectively (inset of Figure 10F). From the results in Figures 10F and 10G, the shielding effectiveness is enhanced with the mesh number increases because of the intensive relative permeability and conductivity of the fabric. Once the ES-HNG is attached around the abdomen of a human for the self-powered health monitor device, the breath rate (Figure 10H) and strength (Figure 10I) can be detected in real time, which broadens the application field effectively.

To date, the traditional multifunctional sensors face a vital problem that the electrical output signals are going to interference and intersection with different input factors, which dramatically hinders the application (Majumder et al., 2019). Depending on the coupling effects of triboelectric and pyroelectric, Shin et al. presented a pressure and temperature multimodal sensor (PTMS) (Shin et al., 2020). As a widely used material for multifunctional sensor devices, the poly (vinylidenefluoride-co-trifluoroethylene) (P(VDF-TrFE)) displayed piezoelectric and pyroelectric effects, and the more important thing is that this material's electrification property can be controlled by changing the applied polarization bias to further switch the dipoles aligned direction. Figure 10J schematically exhibited the diagram of PTMS that the identical material with different polarity is adopted as two friction layers. The working mechanism is shown in Figure 10K that is also based on contact electrification and electrostatic induction during one cycle. As a pressure sensor, the current increases gradually along with the increasing pressure ranging from 98 Pa to 98 kPa (Figure 10L). The response regions can be divided into three according to the difference of sensitivity: 40, 11.5, and 3.7 nA/kPa in the low, middle, and high-pressure regions, respectively (Figure 10M). Particularly, when the temperature applied to the PTMS changes, the degree of dipole oscillation varies and therefore pyroelectricity signals generate, as displayed in Figure 10N. In addition, the degree of dipole oscillation depends on the temperature gradient that the heating state results in a lower level polarization, whereas the cooling state leads to a higher level. The real-time current output to verify the temperature sensing ability is tested for ΔT from -20 to 20°C. As revealed in Figure 10O, the pyroelectric current is closely related to temperature change and is proportional to the absolute value of temperature change. The sensitivity reaches 0.38 and 0.27 nA/°C in the cooling and heating state, which is higher than previous works (Figure 10P). To be noted, the PTMS can detect the pressure and temperature simultaneously without signal interference because they rely on different mechanisms. For example, when the pressure is applied on PTMS with the temperature higher than RT, the electron flow based on triboelectric and pyroelectric is in the same direction, first the sharp triboelectric and gradual pyroelectric signals, as exhibited in Figure 10Q.

Pyroelectric/Piezoelectric Effect

Ferroelectric materials are a kind of important functional material with broad development prospects due to their unique piezoelectric effect, photoelectric effect, pyroelectric effect, and ferroelectric properties (Ismail et al., 2019; Bonnell, 2013). Momentous efforts have been made to exploit the ferroelectric materials in nanogenerators. For instance, Roy et al. introduced a facile approach to design the self-powered multifunctional sensor for pressure and temperature based on graphene oxide (GO) encapsulated PVDF nanofibers that are weaved by electrospinning, as illustrated in Figure 11A (Roy et al., 2019). The commercial Cu-Ni conductive knit polyester fabric is chosen as the double-sided electrode material in order to make the device flexible and wearable (Figure 11B). Finally, the sandwiched structure is enclosed by the PDMS. As presented in Figure 11C, the generated voltage has excellent linear responses with a positive correlation to the pressure and detects the minimum pressure as low as 10 Pa. The device is able to harvest the pyroelectric energy when illuminated by an IR light because of the pyroelectric properties of GO/PVDF composites. As can be seen in Figure 11D, the temperature is dynamically tuned by the IR radiation and convective cooling. The curve of the temperature gradient (dT/dt) is obtained by the derivation of temperature versus time. Convincingly, the tendency of current and voltage performance is highly consistent with the temperature gradient and real-time temperature, respectively (Figure 11E). By attaching the device to an N95 breathing mask and worn over the mouth, the physiological signal of breathing can be recorded due to the temperature fluctuation caused by the human respiratory (Figure 11F).

Similarly, Song et al. also developed a self-powered pressure and temperature sensing system (PTSS) through the adoption of ecofriendly ferroelectric material BTO with conjuncted piezo-pyroelectric effects (Song et al., 2019). It is sandwiched between the Al electrodes and encapsulated by PDMS to form an array with flexibility,

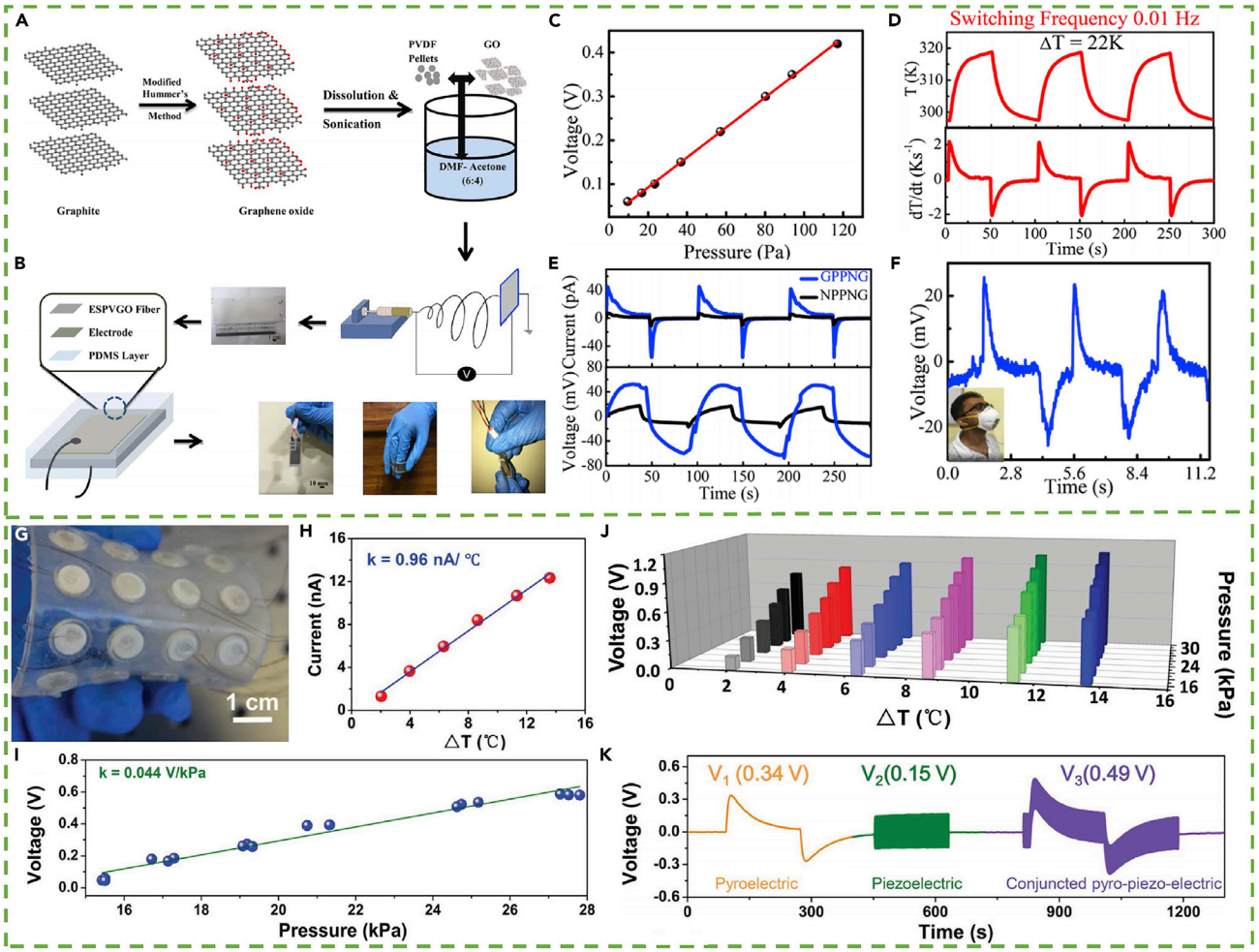

Figure 11. Multifunctional Sensors Based on Pyro/Piezoelectric Effects

(A) The fabrication process of a multifunctional sensor.

(B) The schematic illustration of the device.

(C) The voltage response with respect to pressure.

(D) The dynamically tuned temperature and corresponding temperature gradient.

(E) The current and voltage change along with the tuned temperature.

(F) The physiological signal recording.

(G) The photograph of PTSS array. Reproduced with permission (Roy et al., 2019). Copyright©2019, American Chemical Society.

(H) The current response under different temperature gradients.

(I) The voltage response with pressure.

(J) The electrical signals along with the applied stressing and temperature changes.

(K) The individual and combination of pyroelectric and piezoelectric response. Reproduced with permission (Song et al., 2019). Copyright©2019, Wiley-VCH.

as presented in Figure 11G. To take advantage of the pyroelectric property of BTO, the temperature sensing performance is tested by utilizing a semiconductor heater to control the periodic heating process. As depicted in Figure 11H, there is a perfect linear correlation between current output and temperature gradient with a sensitivity of 0.96 nA/°C. The real-time and accurate temperature value is acquired by analyzing this sensing curve. In addition, the electrical response for the piezoelectric effect is displayed in Figure 11I that the voltage is linearly increased depending on the pressure with the sensitivity of about 44 mV/kPa in the range from 15.4 to 27.6 kPa. In order to demonstrate the sensing stability of pressure and temperature under different conditions of PTSS, the voltage performances under different compression gradients and heating or cooling states are measured. The results in Figure 11J indicate that the electrical signals of the PTSS increase along both with the applied stressing and temperature changes without energy loss. What is more interesting is that the voltage signals of pyroelectric, piezoelectric, and the combined effects are recorded individually. The shapes of voltage are displayed in

Figure 11K: the pyroelectric signal is a sharp peak, whereas the piezoelectric effect results in a relatively gentle continuous peak. The signal of conjuncted effects is also combined and enhanced, intuitively.

Triboelectric Coupled with Other Effects

In recent years, intelligent robots have increasingly entered people's lives and draw tremendous attention. As the connection between intelligent robots and the external environment, smart skin plays an important role and is required to be biomimetic, flexible, and stretchable (Zhao and Zhu, 2018; Han et al., 2018b). For this purpose, Bu et al. designed a triboelectric–photonic smart skin (TPSS), which is able to sense tactile and gesture similar to the human skin (Bu et al., 2018). As displayed in Figure 12A, the structure of TPSS mainly contains the peripheral silicone rubber layer bonded with a layer of grating structure metal film and conducting Ag nanowires network inside. The luminescent powder with aggregation-induced emission character is mixed into the silicon rubber prepolymer for generating the luminescent emission especially exposed to the UV light. The TPSS is easy to attach to the robotic finger (Figure 12B). In general, the cracks of the metal film are harmful to the electronics because of the reduced electrical conductivity and transparency, as shown in the left of Figure 12C. But once stretching the STPS, the metal film will function as a strain depending on the grating to change the exposure area and furtherly regulate the photoluminescence (PL) intensity, as illustrated in the right of Figure 12D. This phenomenon has been experimentally confirmed, which can be seen in Figure 12D that the intensity of PL increases visibly with the elongation of STPS. Quantificationally, the peak intensity boosts three times at 510 nm in the strain of 0%–160%, which is better than traditional strain sensors (Figure 12E). Meanwhile, the electrical outputs under different pressure ranges are measured. The results in Figure 12F revealed that there are three distinct regions according to the sensitivity, and the highest sensitivity reaches 34 mV/Pa at a small pressure range. Furthermore, by integrating the TPSS on five fingers of robot hands, the PL intensity and electrical performance under different gestures can be detected and interpreted at the 3D map. As exhibited in Figure 12G, the signals of gesture "OK" are recorded and translated into readable maps. At the same time, the authors demonstrate that all the tactile sensing is independent and has no signal interference with each other (Figure 12H).

The detection of motion parameters such as moving direction, speed, or acceleration of linear displacement or rotational motion is quite significant to the development of integration devices in IoTs. Wu et al. developed a multifunctional magnet regulation motion sensor (MRMS) working without any power supply (Wu et al., 2018). The MRMS is mainly composed of a TENG with six independent electrodes for generating sensing signals, a regulation system, and an acrylic shell, as expressed in Figure 12I. The arrangement of six electrodes is two annulus electrodes at the inner and outer of the disk and four arc electrodes between them, which are marked as East (E), South (S), West (W), and North (N) directions. The movable magnetic disk (MD) and fixed magnetic cylinder (MC) make up the regulation part. The function of MC is pulling back the MD to the center position by the magnetic force each time, which ensures the accuracy of the next sensing action. The detailed sensing mechanism is exhibited in Figure 12J. When the magnetic disk moves, it comes in contact with the PTFE friction layer at different positions and hence generates a voltage at different electrodes. For instance, Figure 12K is the schematic illustration of the motion in the east direction. By this movement, the voltage of the electrode E is much larger than the others, which indicates the various motion directions successfully (Figure 12L). When rotating the MRMS, the output will generate on electrodes sequentially, and the rotation parameters including direction and speed can be obtained by analyzing the time feather of the voltage waveforms. And more interestingly, the acceleration of linear motion can be detected through the delta-T of the valley and peak values of the inner and outer electrodes due to the fixed distance between them, as illustrated in Figure 12M. The relationships between acceleration and T is exponential reduction (Figure 12N).

Furthermore, Wang et al. designed a self-powered smart sensing network for a multifunctional sensor system based on the flag-like TENG and solar cells (Wang et al., 2017). The structure diagram is exhibited in Figure 12O. A flat Al foil is attached to the polypropylene (PP) substrate and a PTFE film with a rough surface is unilaterally fixed to the specially designed channel for the wind blowing. As the COMSOL simulation result shows in Figure 12P, no matter the PTFE is in flat or flag states, the evident difference of potential distribution between PTFE and Al foil is generated and thus output the electrical signals. For the purpose of converting the wind energy to electricity and sensing the wind speed, the measurement of the voltages under different wind speeds is explored. As clearly expressed in Figure 12Q, the open-circuit voltage values increased linearly with faster speeds, and a shorter period is obtained since the quicker the contact and separation motion. Since the integration of the solar cell in the transparent system by replacing the opaque Al foil and PP substrate with the ITO conductive electrode, it can not only harvest solar energy

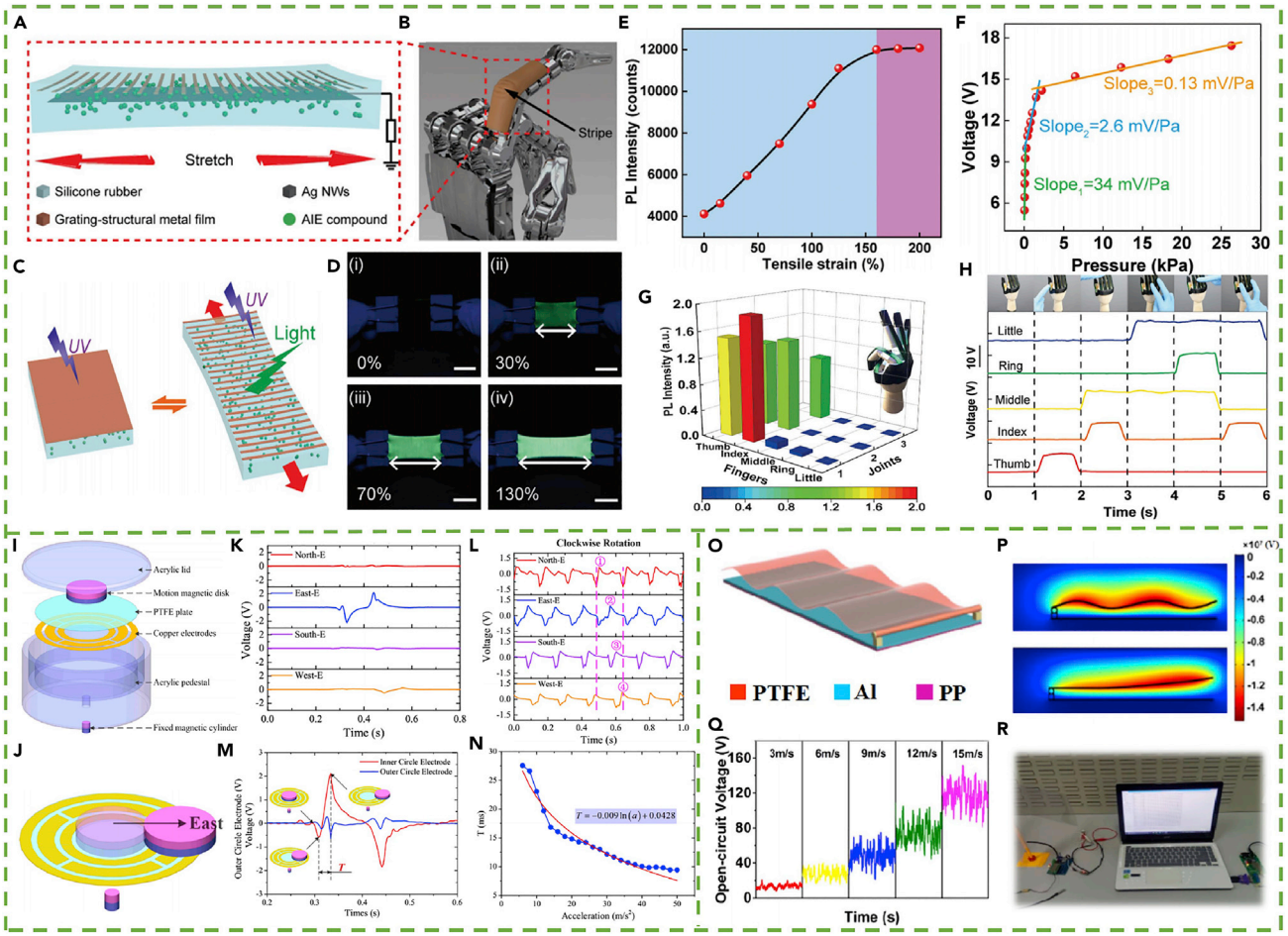

Figure 12. Multifunctional Sensors Based on Triboelectric Coupled with Other Effects

(A) Schematic illustration of the TPSS.

(B) The attachment of TPSS to robotic hands.

(C) The illustration of tunable PL.

(D) The entity graph of PL under stretching.

(E) The PL intensity with different tensile strain.

(F) The voltage response with the pressure stimuli.

(G) The 3D normalized PL intensity of five fingers with the gesture "OK".

(H–J) (H) The voltages of five fingers with different pressing. Reproduced with permission (Bu et al., 2018). Copyright©2018, Wiley-VCH. The structure diagram of MRMS (I) and the motion to the east direction (J).

(K) The electrical response of motion in (J).

(L–N) (L) The response of rotational movement. The data analysis (M) and sensitivity (N) of the acceleration sensor. Reproduced with permission (Wu et al., 2018). Copyright©2018, American Chemical Society.

(O) Schematic illustration of the self-powered smart sensing network.

(P) The simulation results of potential distribution.

(Q) The open-circuit voltages with different wind speeds.

(R) The temperature sensing system. Reproduced with permission (Wang et al., 2017). Copyright©2017, Elsevier.

but can also be used as a temperature sensor. As demonstrated in Figure 12R, the temperature signals can be sent to the computer by the transmitter with the energy storage module for powering.

MULTIFUNCTIONAL SELF-POWERED SENSORS BASED ON MULTIPLE EFFECTS

Triboelectric-Piezoelectric-Pyroelectric Coupled Effects

The research of tactile sensors is of decisive importance for the implementation in various fields, such as smart robotics, bionic skin, or healthcare monitorings. However, the reported tactile sensor is able to

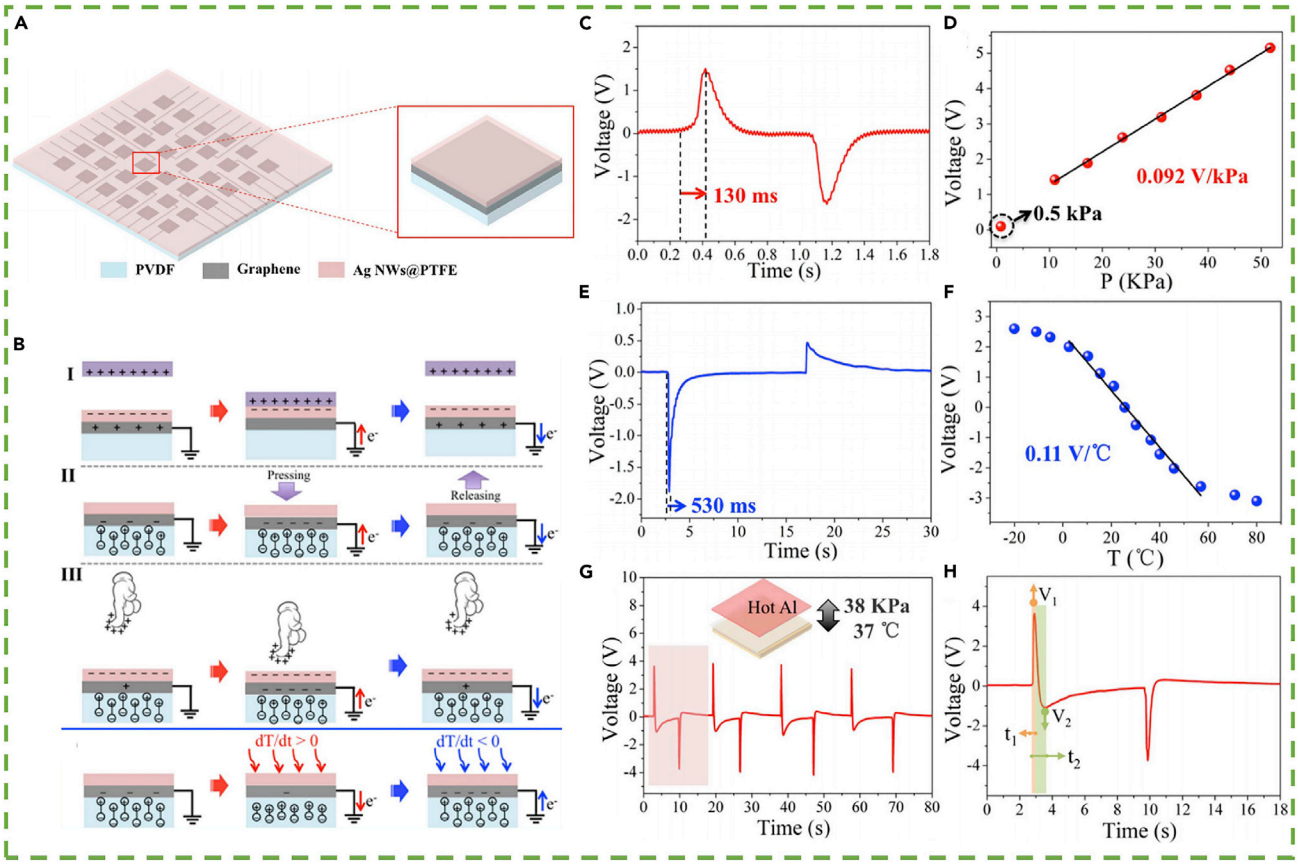

Figure 13. Multifunctional Sensors Based on Triboelectric-Piezoelectric-Pyroelectric Coupled Effects

(A) Schematic illustration of the ab-TS.

(B–F) (B) The working mechanism. The response time (C) and sensitivity (D) as a pressure sensor. The response time (E) and sensitivity (F) as a temperature sensor.

(G) Detection of pressure and temperature, simultaneously.

(H) The enlarged figure of (G). Reproduced with permission (Ma et al., 2019b). Copyright©2019, Elsevier.

detect one stimulating factor at the same time, which is incapable of the real application (Zou et al., 2017; Chi et al., 2018). In order to overcome the above shortcomings, Ma et al. introduced an active flexible antibacterial tactile sensor (ab-TS) based on the multiple effects, including triboelectric, piezoelectric, and pyroelectric, for distinguishing different stimuli (Ma et al., 2019b). The detailed structure of ab-TS is expressed in Figure 13A. It is a sandwiched arrangement that the conductive graphene is inside and the PTFE doped with the Ag nanowires for antibacterial function at the top and PVDF film at the bottom. The PTFE owns the excellent triboelectric property, and PVDF is a widespread material choice for the fulfillment of piezoelectric and pyroelectric effects. The sensing principles of pressure and temperature are illustrated in Figure 13B. Triboelectric and piezoelectric both serve for pressure detection, and they can work independently (I and II) or enhanced coupling (III). The PVDF is going to reach a high-level polarization once compressing on it, and then the electrons will flow from the ground to the graphene electrode. In addition, the PVDF responds to the temperature gradient for the human finger and ab-TS due to the pyroelectric effects. Similarly, the density of polarization decreases when the temperature rises as the reduction of dipole moments and expanded volumes. The sensing performance of pressure is displayed in Figures 13C and 13D. The response time is about 130 ms by the interval of signal generating and reaches the peak. The sensitivity is 0.092 V/kPa at the range of 10.5–52 kPa with the smallest detectable pressure of 0.5 kPa. As shown in Figures 13E and 13F, the response time is approximately 530 ms as a temperature sensor and the sensitivity is 0.11 V/°C with a perfect negative correlation when the temperature changes from 10 to 45°C. In the condition that both pressure and higher temperature are applied, the voltage waveform is exhibited in Figure 13G. There are two distinct peaks with

opposite directions generated in succession. It is noted in the enlarged figure (Figure 13G) that the positive peak is narrower and sharp, whereas the negative is wider and slow. This is consistent with the response time of different effect mechanisms that the response time of pyroelectric nanogenerator is longer than the others. Based on this principle, the sensing of pressure and temperature can be separated by the difference of response time, which enables the fulfillment of a multifunctional sensor without signal interaction.

Photovoltaic–Pyroelectric–Piezoelectric Coupled Effects

Nowadays, ferroelectric materials have obtained plenty of attention in the energy harvesting field due to their photovoltaic, pyroelectric, and piezoelectric effects (Zhao et al., 2020). In particular, BTO possesses a high piezoelectric constant with non-toxic and environmentally friendly. In 2019, Ji et al. utilized the BTO material to fabricate the one-structure-based self-powered sensing device by the mechanism of coupling photovoltaic–pyroelectric–piezoelectric effects (Ji et al., 2019). As displayed in Figure 14A, the device mainly includes a BTO ceramic slice sandwiched between an interdigitated ITO and Ag film electrodes with one end fixed onto the thermoelectric module for temperature control. A mass block is attached to another end of BTO for signal enhancement when sensing vibration parameters. Figure 14B revealed the current performance of the device with single stimulated such as light, temperature, or vibration. The current waveforms have a sharp peak caused by pyroelectric effect $I_{Pyro+Photo}$ and a stable platform due to the bulk photovoltaic influence I_{Photo} (Figure 14B-i). It is interesting that $I_{Pyro+Photo}$ and I_{Photo} increase all linearly as the light intensifies (Figure 14B-ii), demonstrating the feasibility of the device in light sensing. As presented in Figure 14B-iii, the device is capable of detecting the temperature difference ΔT with a positive correlation of current I_{Pyro}. The I_{Pyro}–ΔT curve can be divided into two regions that the sensitivity is 4.8 nA/K at the cooling process while 1.75 nA/K at the heating condition (Figure 14B-iv). That is probably because the electrical dipoles are going to oscillating randomly and differently at low and high temperatures. Furthermore, the vibration-frequency-dependent relation is measured. As displayed in Figure 14B-v, the current increases firstly with the frequency increases but then decreases after the frequency is larger than 17 Hz. The corresponding sensitivity is obtained by the I_{Piezo}–*frequency* curve (Figure 14B-vi) that is 21.02 nA/Hz and −14.07 nA/Hz, respectively. To demonstrate the ability to sense multiple signals simultaneously, the authors also test the outputs under light + cooling/heating (Figure 14C), cooling/heating + vibration (Figure 14D) conditions, and even all the three kinds of stimulation (Figures 14E and 14F). It is important to draw the conclusion that the device keeps always a linear relationship with different other factor influence and is quite stable for light intensity, temperature change, and vibration sensing individually or simultaneously. It is of the extraordinary significance of this work in a self-powered multifunctional sensor based on hybrid nanogenerators.

CONCLUSIONS AND PERSPECTIVES

In summary, this review systematically introduced the latest progress on the multifunctional self-powered sensor based on the HNG. Nanogenerators mainly include TENG, PENG, and PyENG that can convert external energy into electricity. Among them, TENG has the unique advantages of extensive material adoption and various structure design. Consequently, the principles and prototypes of multifunctional self-powered sensors based on TENG are firstly summarized. In order to avoid signal interference and energy insufficient, the multifunctional self-powered sensors based on HNG were reviewed in the subsequent section. However, despite the rapid progress that has been made about the multifunctional self-powered sensors based on HNG, there are still some issues unaddressed that hinder the development. One is how to realize sensing signal recognition based on as few modules as possible. Most of the existing multifunctional sensors test under a single variable rather than multiple variables simultaneously. This is inconsistent with the real application scenarios. If multiple factors change at the same time, how to distinguish signal sources becomes a difficult problem to solve. Moreover, how to miniaturize the whole IoT system such as sharing a common back-end processing circuit without signal interference is another issue that needs to be solved further. Another challenge is how to supply the power for the whole IoT system. Until now, the description of "self-powered" is only related to sensors. It is still unrealistic for the entire IoT system to work without any power supply. So, it is urgent and meaningful to develop multifunctional self-powered IoT systems by combining the ability of hybridized nanogenerators that can not only sense but also harvest energy from the external environments. Besides, further research needs to be conducted eagerly for promoting the practical application in IoTs field, especially the following aspects (expressed in Figure 15):

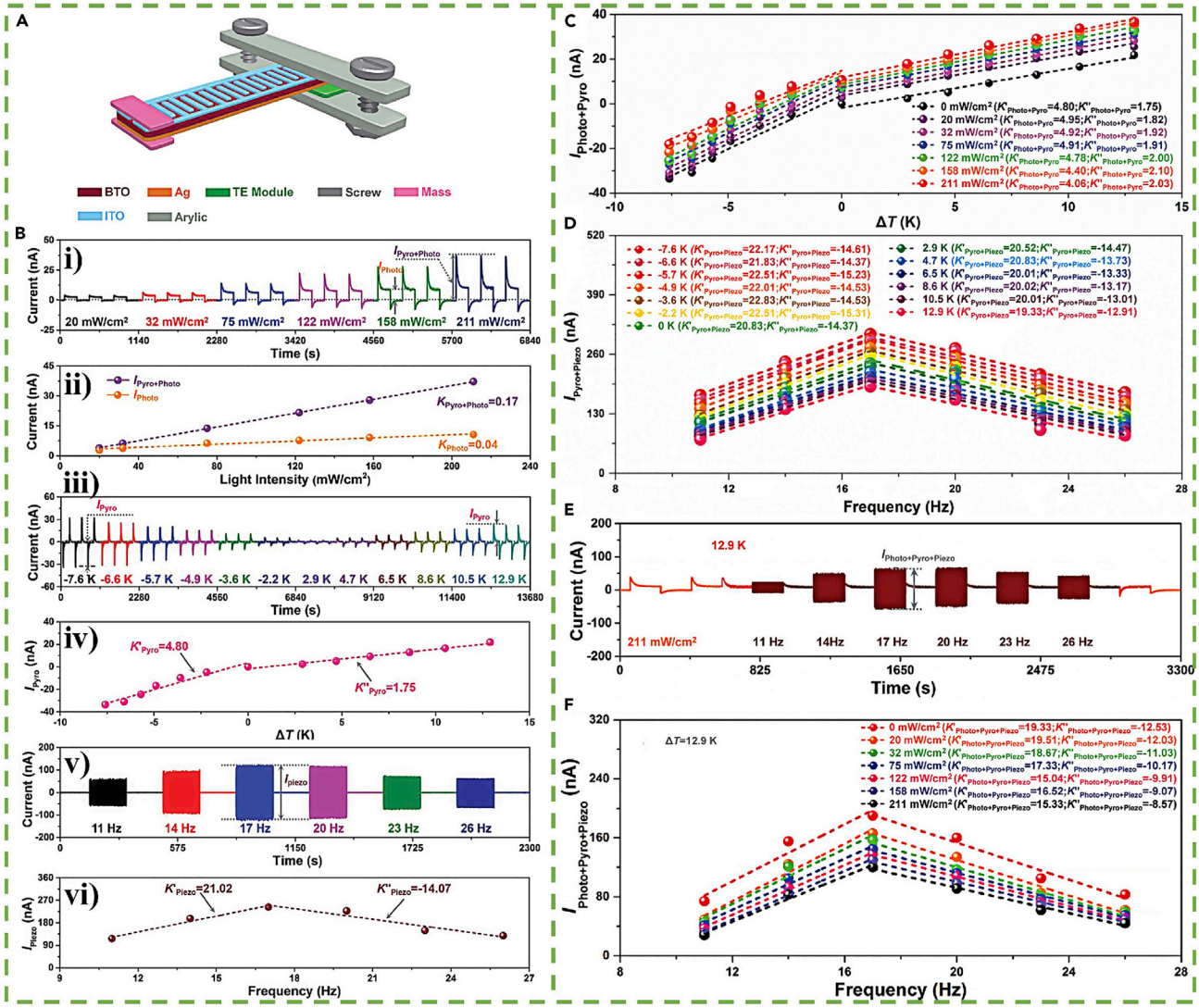

Figure 14. Multifunctional Sensors Based on Photovoltaic–Pyroelectric–Piezoelectric Coupled Effects

(A) Schematic illustration of the one-structure-based self-powered sensing device.

(B) The real-time current and sensitivity of the stimulation light intensity, temperature change, and vibration frequency.

(C) The relationship between current and temperature changes under different light illuminations.

(D) The relationship between current and vibration frequency under different temperature variations.

(E) The current response under light + heating + vibration conditions.

(F) The relationship between current and vibration frequency under different light intensities. Reproduced with permission (Ji et al., 2019). Copyright©2019, Wiley-VCH.

1. High-quality sensors: if the data information collected by the sensor is wrong, it is equivalent to the error at the source, and the transmission, analysis, and application of all subsequent data will be meaningless. Therefore, the accuracy and resolution of the sensor are the important baselines to ensure the vision of the IoTs. In addition, considering that the sensors need to work continuously for quite a long time, stability and durability are elementary requirements for practical applications.

2. Integration: on the one hand, the integration of different functions into one sensor device is crucially important for the wider perception range. On the other hand, the integration of sensors with the power management section, software platform, as well as wireless communication modular is a deeply effective alternative to reach the implementation of IoTs.

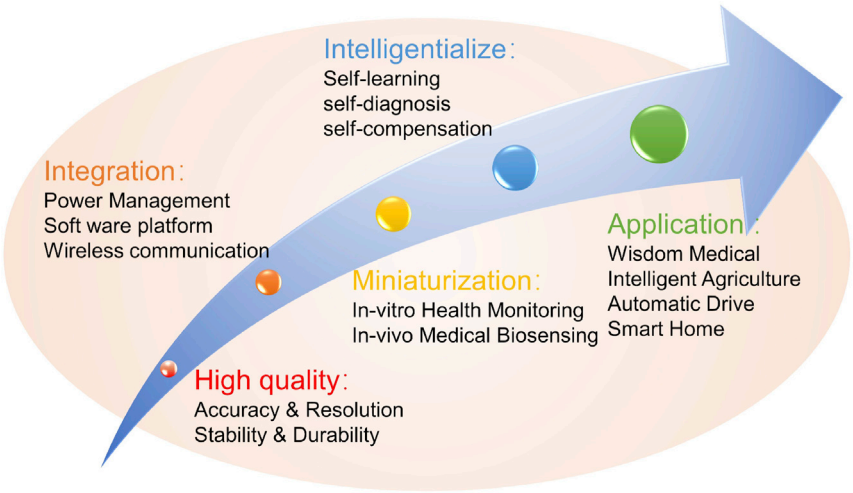

Figure 15. Future Development of Sensors in the IoTs

3. Miniaturization: sometimes the human is an important part of IoTs; it is inevitable that some devices are possibly wearable equipment *in vitro* for health monitoring or even need to be implanted *in vivo* for medical biosensing. Under these circumstances, a smaller volume of sensors is the primary demand and extremely beneficial for users to get a comfortable experience. At the same time, the miniaturization of sensors is significant for the integration with electronic devices, especially considering the huge number of sensors adopted.
4. Intelligentialize: as an edge node in the IoTs, the sensors are necessary to integrate with a microprocessor in order to form an intelligent data terminal device with the functions of environment perception, data processing, and intelligent control. The system has the capability of self-learning, self-diagnosis, and self-compensation. In this way, when sensors perceive the physical world, the data fed back to the IoTs system will be more accurate and comprehensive, so as to achieve the purpose of accurate perception.
5. More application scenarios: with the advancement of hardware equipment and software implementation technology, IoTs will be more and more widely applied in more application scenarios. In particular, wisdom medical, intelligent agriculture, automatic drive, and smart home are the most populating fields over the next few decades. Consequently, more pertinent and professional sensors will be developed in the future.

ACKNOWLEDGMENTS

This work was financially supported by the National Science and Technology Major Project from Minister of Science and Technology of China (Grant No. 2018AAA0103104), National Natural Science Foundation of China (NSFC) (No. 61804103), Natural Science Foundation of the Jiangsu Higher Education Institutions of China (No. 18KJA535001), Jiangsu Key Laboratory for Carbon-Based Functional Materials & Devices, Soochow University (KJS1803), and the XJTLU Key Program Special Fund (KSF-A-18), Research and Development of Inkjet Technology and Nozzle Devices (NO. Y8AAY11001), and Research on MEMS Piezoelectric Nozzle for Powder Bonded 3D Printer (SYG201632). This work is also supported by the Collaborative Innovation Center of Suzhou Nano Science & Technology, the Priority Academic Program Development of Jiangsu Higher Education Institutions (PAPD), the 111 Project, and Joint International Research Laboratory of Carbon-Based Functional Materials and Devices.

AUTHOR CONTRIBUTIONS

Conceptualization, T. Zhang and Z. Wen; Investigation, Y. Liu and Z. Zhang; Writing—Original Draft, T. Zhang; Writing—Review & editing, T. Zhang and Z. Wen; Supervision, Z. Wen; Funding Acquisition, Y. Xie and X. Sun.

REFERENCES

Abbasi, W.A., Wang, Z., Zhou, Y., and Hassan, S. (2019). Research on measurement of supply chain finance credit risk based on internet of things. Int. J. Distrib. Sens. Netw. *15*, 1550147719874002.

Abdel-Basset, M., Manogaran, G., Mohamed, M., and Rushdy, E. (2019). Internet of things in smart education environment: supportive framework in the decision-making process. Concurrency. Comput. Pract. Exp. *31*, e4515.

Ahmed, A., Hassan, I., Mosa, I.M., Elsanadidy, E., Sharafeldin, M., Rusling, J.F., and Ren, S. (2019). An ultra-shapeable, smart sensing platform based on a multimodal ferrofluid-infused surface. Adv. Mater. *31*, 1807201.

Al-Fuqaha, A., Guizani, M., Mohammadi, M., Aledhari, M., and Ayyash, M. (2015). Internet of things: a survey on enabling technologies, protocols, and applications. IEEE Commun. Surv. Tutor. *17*, 2347–2376.

Alva, G., Liu, L., Huang, X., and Fang, G. (2017). Thermal energy storage materials and systems for solar energy applications. Renew. Sustain. Energy Rev. *68*, 693–706.

Ankerhold, U., Hupe, O., and Ambrosi, P. (2009). Deficiencies of active electronic radiation protection dosemeters in pulsed fields. Radiat. Prot. Dosimetry *135*, 149–153.

Askari, H., Hashemi, E., Khajepour, A., Khamesee, M.B., and Wang, Z. (2018). Towards self-powered sensing using nanogenerators for automotive systems. Nano Energy *53*, 1003–1019.

Atzori, L., Iera, A., and Morabito, G. (2010). The internet of things: a survey. Comput. Netw. *54*, 2787–2805.

Berglund, E.Z., Monroe, J.G., Ahmed, I., Noghabaei, M., Do, J., Pesantez, J.E., Fasaee, M.A.K., Bardaka, E., Han, K., Proestos, G.T., et al. (2020). Smart infrastructure: a vision for the role of the civil engineering profession in smart cities. J. Infrastruct. Syst. *26*, 03120001.

Bonnell, D.A. (2013). Ferroelectric organic materials catch up with oxides. Science *339*, 401–402.

Bu, T., Xiao, T., Yang, Z., Liu, G., Fu, X., Nie, J., Guo, T., Pang, Y., Zhao, J., Xi, F., et al. (2018). Stretchable triboelectric-photonic smart skin for tactile and gesture sensing. Adv. Mater. *30*, 1800066.

Byun, K.E., Cho, Y., Seol, M., Kim, S., Kim, S.W., Shin, H.J., Park, S., and Hwang, S. (2016). Control of triboelectrification by engineering surface dipole and surface electronic state. ACS Appl. Mater. Interfaces *8*, 18519–18525.

Chang, C., Srirama, S.N., and Buyya, R. (2017). Indie fog: an efficient fog-computing infrastructure for the internet of things. Computer *50*, 92–98.

Chau, C.K., Qin, F., Sayed, S., Wahab, M.H., and Yang, Y. (2010). Harnessing battery recovery effect in wireless sensor networks: experiments and analysis. IEEE J. Sel. Areas Commun. *28*, 1222–1232.

Chen, J., and Yang, A. (2019). Intelligent agriculture and its key technologies based on internet of things architecture. IEEE Access *7*, 77134–77141.

Chen, S., Tao, X., Zeng, W., Yang, B., and Shang, S. (2017). Quantifying energy harvested from contact-mode hybrid nanogenerators with cascaded piezoelectric and triboelectric units. Adv. Energy Mater. *7*, 1601569.

Chen, Y., Wang, Y., Zhang, Y., Zou, H., Lin, Z., Zhang, G., Zou, C., and Wang, Z.L. (2018a). Elastic-beam triboelectric nanogenerator for high-performance multifunctional applications: sensitive scale, acceleration/force/vibration sensor, and intelligent keyboard. Adv. Energy Mater. *8*, 1802159.

Chen, B., Tang, W., He, C., Jiang, T., Xu, L., Zhu, L., Gu, G., Chen, J., Shao, J., Luo, J., et al. (2018b). Ultrafine capillary-tube triboelectric nanogenerator as active sensor for microliquid biological and chemical sensing. Adv. Mater. Technol. *3*, 1700229.

Chen, X., Ren, Z., Han, M., Wan, J., and Zhang, H. (2020). Hybrid energy cells based on triboelectric nanogenerator: from principle to system. Nano Energy *75*, 104980.

Cheng, L., Xu, Q., Zheng, Y., Jia, X., and Qin, Y. (2018). A self-improving triboelectric nanogenerator with improved charge density and increased charge accumulation speed. Nat. Commun. *9*, 3773.

Chi, C., Sun, X., Xue, N., Li, T., and Liu, C. (2018). Recent progress in technologies for tactile sensors. Sensors *18*, 948.

Cui, X., Ni, X., and Zhang, Y. (2016). Theoretical study of output of piezoelectric nanogenerator based on composite of pzt nanowires and polymers. J. Alloy. Compd. *675*, 306–310.

Duan, Z., Jiang, Y., Yan, M., Wang, S., Yuan, Z., Zhao, Q., Sun, P., Xie, G., Du, X., and Tai, H. (2019). Facile, flexible, cost-saving, and environment-friendly paper-based humidity sensor for multifunctional applications. ACS Appl. Mater. Interfaces *11*, 21840–21849.

Duggen, L., Willatzen, M., and Wang, Z.L. (2018). Mechanically bent graphene as an effective piezoelectric nanogenerator. J. Phys. Chem. C *122*, 20581–20588.

Eric, B., Houlleberghs, M., Radhakrishnan, S., Gruebel, G., Taulelle, F., and Martens, J.A. (2020). Water as a tuneable solvent: a perspective. Chem. Soc. Rev. *49*, 2557–2569.

E, S., Zhang, Y., Wang, X., Zhang, Y., and Han, B. (2019). Capillary encapsulated reflective fiber optic spr temperature sensor. Phys. Scr. *94*, 045504.

Fan, F., Tian, Z., and Wang, Z.L. (2012a). Flexible triboelectric generator. Nano Energy *1*, 328–334.

Fan, F., Lin, L., Zhu, G., Wu, W., Zhang, R., and Wang, Z.L. (2012b). Transparent triboelectric nanogenerators and self-powered pressure sensors based on micropatterned plastic films. Nano Lett. *12*, 3109–3114.

Fan, F., Tang, W., and Wang, Z. (2016). Flexible nanogenerators for energy harvesting and self-powered electronics. Adv. Mater. *28*, 4283–4305.

Ferrandez-Pastor, F.J., Garcia-Chamizo, J.M., Nieto-Hidalgo, M., Mora-Pascual, J., and Mora-Martinez, J. (2016). Developing ubiquitous sensor network platform using internet of things: application in precision agriculture. Sensors *16*, 1141.

Fong, D.T.P., and Chan, Y. (2010). The use of wearable inertial motion sensors in human lower limb biomechanics studies: a systematic review. Sensors *10*, 11556–11565.

Fu, Y., Li, W., Chen, S., Wang, Z., and Liu, Y. (2020). Experimental and simulation study on the capacitive liquid level gauge of lng vehicular cylinder. Measurement *164*, 107930.

Gao, Z., Zhou, J., Gu, Y., Fei, P., Hao, Y., Bao, G., and Wang, Z.L. (2009). Effects of piezoelectric potential on the transport characteristics of metal-zno nanowire-metal field effect transistor. J. Appl. Phys. *105*, 113707.

Gardasevic, G., Katzis, K., Bajic, D., and Berbakov, L. (2020). Emerging wireless sensor networks and internet of things technologies-foundations of smart healthcare. Sensors *20*, 3619.

Gil, D., Ferrandez, A., Mora-Mora, H., and Peral, J. (2016). Internet of things: a review of surveys based on context aware intelligent services. Sensors *16*, 1069.

Givoni, B., Khedari, J., Wong, N.H., Feriadi, H., and Noguchi, M. (2006). Thermal sensation responses in hot, humid climates: effects of humidity. Build. Res. Informat. *34*, 496–506.

Goncharuk, V.V., Rudenko, A.V., Saprykina, M.N., and Bolgova, E.S. (2018). Detection of microorganisms in nonculturable state in chlorinated water. J. Water Chem. Technol. *40*, 40–45.

Greason, W.D. (2012). Triboelectrification of wood. IEEE Trans. Ind. Appl. *48*, 1177–1181.

Grover, A., and Lall, B. (2020). A novel method for removing baseline drifts in multivariate chemical sensor. IEEE Trans. Instrum. Meas. *69*, 7306–7316.

Guo, L. (2017). Design and implementation of logistics information system based on internet of things. Agro Food Ind. Hi Tech *28*, 2646–2651.

Guo, H., Chen, J., Tian, L., Leng, Q., Xi, Y., and Hu, C. (2014). Airflow-induced triboelectric nanogenerator as a self-powered sensor for detecting humidity and airflow rate. ACS Appl. Mater. Interfaces *6*, 17184–17189.

Guo, H., Li, T., Cao, X., Xiong, J., Jie, Y., Willander, M., Cao, X., Wang, N., and Wang, Z. (2017). Self-sterilized flexible single-electrode triboelectric nanogenerator for energy harvesting and dynamic force sensing. ACS Nano *11*, 856–864.

Guo, R., Wang, X., Yu, W., Tang, J., and Liu, J. (2018). A highly conductive and stretchable wearable liquid metal electronic skin for long-term conformable health monitoring. Sci. China Technol. Sci. *61*, 1031–1037.

Guo, J., Cheng, G., and Du, Z. (2020). The recent progress of triboelectric nanogenerator-assisted photodetectors. Nanotechnology *31*, 292003.

Han, C., Lin, Q., Guo, J., Sun, L., and Tao, Z. (2018a). A clustering algorithm for heterogeneous wireless sensor networks based on solar energy supply. Electronics *7*, 103.

Han, L., Ding, J., Wang, S., Xu, J., Yuan, N., Cheng, G., and Liu, Z. (2018b). Multi-functional stretchable and flexible sensor array to determine the location, shape, and pressure: application in a smart robot. Sci. China Technol. Sci. *61*, 1137–1143.

He, F., You, X., Gong, H., Yang, Y., Bai, T., Wang, W., Guo, W., Liu, X., and Ye, M. (2020). Stretchable, biocompatible, and multifunctional silk fibroin-based hydrogels toward wearable strain/pressure sensors and triboelectric nanogenerators. ACS Appl. Mater. Interfaces *12*, 6442–6450.

Henriques, I.B., Keutenedjian Mady, C.E., and De Oliveira Junior, S. (2017). Assessment of thermal comfort conditions during physical exercise by means of exergy analysis. Energy *128*, 609–617.

Herman, A., and Herman, A.P. (2019). Antimicrobial peptides activity in the skin. Skin Res. Technol. *25*, 111–117.

Indira, S.S., Vaithilingam, C.A., Oruganti, K.S.P., Mohd, F., and Rahman, S. (2019). Nanogenerators as a sustainable power source: state of art, applications, and challenges. Nanomaterials *9*, 773.

Ismail, M., Wu, Z., You, H., Jia, Y., Xia, J., and Wang, Y. (2019). Photovoltaic effect of "ferroelectric" bananas. EPL *125*, 47001.

Jang, J., Jun, Y.S., Seo, H., Kim, M., and Park, J.U. (2020). Motion detection using tactile sensors based on pressure-sensitive transistor arrays. Sensors *20*, 3264.

Ji, Y., Wang, Y., and Yang, Y. (2019). Photovoltaic–pyroelectric–piezoelectric coupled effect induced electricity for self-powered coupled sensing. Adv. Electron. Mater. *5*, 1900195.

Jian, L., Ning, L., Yang, S., Wang, J., and Hua, M. (2009). Triboelectrification electrostatic potential of mc nylon 6 under point contact dry sliding. Tribol. Lett. *36*, 199–208.

Jian, L., Ning, L., Yang, S., Wang, J., and Hua, M. (2010). Triboelectrification electrostatic potential of graphite/monomer casting nylon composites under dry sliding: correlation with electrical resistivity and wear mechanisms. Polym. Compos. *31*, 1369–1377.

Jiang, D., Su, Y., Wang, K., Wang, Y., Xu, M., Dong, M., and Chen, G. (2020). A triboelectric and pyroelectric hybrid energy harvester for recovering energy from low-grade waste fluids. Nano Energy *70*, 104459.

Jin, M., Zhang, Q., Wang, H., and Yuan, Y. (2020). Research on intelligent transportation system based on internet of things. Int. J. Heavy Veh. Syst. *27*, 247–257.

Jing, Q., Vasilakos, A.V., Wan, J., Lu, J., and Qiu, D. (2014). Security of the internet of things: perspectives and challenges. Wirel. Netw. *20*, 2481–2501.

Khalifa, M., Mahendran, A., and Anandhan, S. (2019). Synergism of graphitic-carbon nitride and electrospinning on the physico-chemical characteristics and piezoelectric properties of flexible poly(vinylidene fluoride) based nanogenerator. J. Polym. Res. *26*, 73.

Khan, A.A., Mahmud, A., and Ban, D. (2019). Evolution from single to hybrid nanogenerator: a contemporary review on multimode energy harvesting for self-powered electronics. IEEE Trans. Nanotechnol. *18*, 21–36.

Kim, S.M. (2018). Theoretical study on the oscillatory triboelectric charge density in a contact-mode triboelectric nanogenerator. Eur. Phys. J. Plus *133*, 535.

Kim, J., Lee, J.H., Ryu, H., Lee, J.H., Khan, U., Kim, H., Kwak, S.S., and Kim, S.W. (2017). High-performance piezoelectric, pyroelectric, and triboelectric nanogenerators based on p(vdf-trfe) with controlled crystallinity and dipole alignment. Adv. Funct. Mater. *27*, 1700702.

Kim, W., Choi, D., Kwon, J.Y., and Choi, D. (2018). A self-powered triboelectric microfluidic system for liquid sensing. J. Mater. Chem. A *6*, 14069–14076.

Kim, S.W., Lee, K.J., and Wang, Z.L. (2019). Nanogenerators and piezo/tribo-tronics. Nano Energy *61*, 637–638.

Kuncoro, C.B.D., Sung, M.F., and Kuan, Y.D. (2019). Battery charger prototype design for tire pressure sensor battery recharging. Sensors *19*, 124.

Lai, Y.C., Hsiao, Y.C., Wu, H.M., and Wang, Z. (2019). Waterproof fabric-based multifunctional triboelectric nanogenerator for universally harvesting energy from raindrops, wind, and human motions and as self-powered sensors. Adv. Sci. *6*, 1801883.

Lee, K.Y., Kim, S.K., Lee, J.H., Seol, D., Gupta, M.K., Kim, Y., and Kim, S.W. (2016). Controllable charge transfer by ferroelectric polarization mediated triboelectricity. Adv. Funct. Mater. *26*, 3067–3073.

Li, X. (2013). Research on water microorganism recognition based on bp neural network algorithm. J. Pure Appl. Microbiol. *7*, 1989–1994.

Li, X. (2019). Research on tourism industrial cluster and information platform based on internet of things technology. Int. J. Distrib. Sens. Netw. *15*, 1550147719858840.

Liegeard, J., and Manning, L. (2020). Use of intelligent applications to reduce household food waste. Crit. Rev. Food Sci. Nutr. *60*, 1048–1061.

Lin, Z., Chen, J., and Yang, J. (2016). Recent progress in triboelectric nanogenerators as a renewable and sustainable power source. J. Nanomater. *2016*, 5651613.

Lin, Z., He, Q., Xiao, Y., Zhu, T., Yang, J., Sun, C., Zhou, Z., Zhang, H., Shen, Z., Yang, J., et al. (2018). Flexible timbo-like triboelectric nanogenerator as self-powered force and bend sensor for wireless and distributed landslide monitoring. Adv. Mater. Technol. *3*, 1800144.

Liu, Y., Feng, L., Liu, S., and Sun, M. (2018). Sensor network oriented human motion segmentation with motion change measurement. IEEE Access *6*, 9281–9291.

Ma, C., and Yang, Y. (2006). Battery-aware routing for streaming data transmissions in wireless sensor networks. Mobile Netw. Appl. *11*, 499–508.

Ma, M., Liao, Q., Zhang, G., Zhang, Z., Liang, Q., and Zhang, Y. (2015). Self-recovering triboelectric nanogenerator as active multifunctional sensors. Adv. Funct. Mater. *25*, 6489–6494.

Ma, N., Zhang, K., and Yang, Y. (2017). Photovoltaic-pyroelectric coupled effect induced electricity for self-powered photodetector system. Adv. Mater. *29*, 1703694.

Ma, Z., Li, S., Wang, H., Cheng, W., Li, Y., Pan, L., and Shi, Y. (2019a). Advanced electronic skin devices for healthcare applications. J. Mater. Chem. B *7*, 173–197.

Ma, M., Zhang, Z., Zhao, Z., Liao, Q., Kang, Z., Gao, F., Zhao, X., and Zhang, Y. (2019b). Self-powered flexible antibacterial tactile sensor based on triboelectric-piezoelectric-pyroelectric multi-effect coupling mechanism. Nano Energy *66*, 104105.

Ma, L., Zhou, M., Wu, R., Patil, A., Gong, H., Zhu, S., Wang, T., Zhang, Y., Shen, S., Dong, K., et al. (2020). Continuous and scalable manufacture of hybridized nano-micro triboelectric yarns for energy harvesting and signal sensing. ACS Nano *14*, 4716–4726.

Maity, K., Mahanty, B., Sinha, T.K., Garain, S., Biswas, A., Ghosh, S.K., Manna, S., Ray, S.K., and Mandal, D. (2017). Two-dimensional piezoelectric mos2-modulated nanogenerator and nanosensor made of poly(vinlydine fluoride) nanofiber webs for self-powered electronics and robotics. Energy Technol. *5*, 234–243.

Majumder, B.D., Roy, J.K., and Padhee, S. (2019). Recent advances in multifunctional sensing technology on a perspective of multi-sensor system: a review. IEEE Sens. J. *19*, 1204–1214.

Mandourarakis, I., and Koutroulis, E. (2018). Unified system- and circuit-level optimization of res-based power-supply systems for the nodes of wireless sensor networks. IEEE Trans. Ind. Inf. *14*, 598–607.

Mikusz, M., Clinch, S., Jones, R., Harding, M., Winstanley, C., and Davies, N. (2015). Repurposing web analytics to support the iot. Computer *48*, 42–49.

Nakatani, Y., Wakamatsu, K., Shindo, T., and Ito, Y. (2009). The status of thermoelectric generation system. IEEJ Trans. Electr. Electron. Eng. *4*, 4–5.

Niu, S., Zhou, Y., Wang, S., Liu, Y., Lin, L., Bando, Y., and Wang, Z.L. (2014). Simulation method for optimizing the performance of an integrated triboelectric nanogenerator energy harvesting system. Nano Energy *8*, 150–156.

Nour, E.S., Khan, A., Nur, O., and Willander, M. (2014). A flexible sandwich nanogenerator for harvesting piezoelectric potential from single crystalline zinc oxide nanowires. Nanomater. Nanotechnol. *4*, 24.

Oh, J.Y., and Bao, Z. (2019). Second skin enabled by advanced electronics. Adv. Sci. *6*, 1900186.

Oztemel, E., and Gursev, S. (2020). Literature review of industry 4.0 and related technologies. J. Intell. Manuf. *31*, 127–182.

Park, K.I., Xu, S., Liu, Y., Hwang, G.T., Kang, S.J.L., Wang, Z.L., and Lee, K.J. (2010). Piezoelectric batio3 thin film nanogenerator on plastic substrates. Nano Lett. *10*, 4939–4943.

Park, S.J., Seol, M.L., Jeon, S.B., Kim, D., Lee, D., and Choi, Y.K. (2015). Surface engineering of triboelectric nanogenerator with an electrodeposited gold nanoflower structure. Sci. Rep. *5*, 13866.

Park, J., Lee, Y., Ha, M., Cho, S., and Ko, H. (2016). Micro/nanostructured surfaces for self-powered and multifunctional electronic skins. J. Mater. Chem. B *4*, 2999–3018.

Peng, Y., Que, M., Tao, J., Wang, X., Lu, J., Hu, G., Wan, B., Xu, Q., and Pan, C. (2018). Progress in piezotronic and piezo-phototronic effect of 2d materials. 2d Mater. *5*, 042003.

Potyrailo, R.A. (2016). Multivariable sensors for ubiquitous monitoring of gases in the era of internet of things and industrial internet. Chem. Rev. *116*, 11877–11923.

Pradilla, J., Esteve, M., and Palau, C. (2018). Sosful: sensor observation service (sos) for internet of things (iot). IEEE Lat. Am. Trans. *16*, 1276–1283.

Proto, A., Penhaker, M., Conforto, S., and Schmid, M. (2017). Nanogenerators for human body energy harvesting. Trends Biotechnol. *35*, 610–624.

Psenakova, Z., and Hudecova, J. (2009). Influence of electromagnetic fields by electronic implants in medicine. Elektron. Elektrotech. *7*, 37–40.

Qi, K., He, J., Wang, H., Zhou, Y., You, X., Nan, N., Shao, W., Wang, L., Ding, B., and Cui, S. (2017). A highly stretchable nanofiber-based electronic skin with pressure-, strain-, and flexion-sensitive properties for health and motion monitoring. ACS Appl. Mater. Interfaces *9*, 42951–42960.

Qian, C., Li, L., Gao, M., Yang, H., Cai, Z., Chen, B., Xiang, Z., Zhang, Z., and Song, Y. (2019). All-printed 3d hierarchically structured cellulose aerogel based triboelectric nanogenerator for multi-functional sensors. Nano Energy *63*, 103885.

Rao, J., Chen, Z., Zhao, D., Ma, R., Yi, W., Zhang, C., Liu, D., Chen, X., Yang, Y., Wang, X., et al. (2020). Tactile electronic skin to simultaneously detect and distinguish between temperature and pressure based on a triboelectric nanogenerator. Nano Energy *75*, 105073.

Ren, X., Fan, H., Wang, C., Ma, J., Lei, S., Zhao, Y., Li, H., and Zhao, N. (2017). Magnetic force driven noncontact electromagnetic-triboelectric hybrid nanogenerator for scavenging biomechanical energy. Nano Energy *35*, 233–241.

Roth, K., and Brodrick, J. (2009). Seasonal energy storage. Ashrae J. *51*, 41–43.

Roy, K., Ghosh, S.K., Sultana, A., Garain, S., Xie, M., Bowen, C.R., Henkel, K., Schmeißer, D., and Mandal, D. (2019). A self-powered wearable pressure sensor and pyroelectric breathing sensor based on go interfaced pvdf nanofibers. ACS Appl. Nano Mater. *2*, 2013–2025.

Ruth, S.R.A., Beker, L., Tran, H., Feig, V.R., Matsuhisa, N., and Bao, Z. (2020). Rational design of capacitive pressure sensors based on pyramidal microstructures for specialized monitoring of biosignals. Adv. Funct. Mater. *30*, 1903100.

Ryu, H., and Kim, S.W. (2019). Emerging pyroelectric nanogenerators to convert thermal energy into electrical energy. Small *15*, 1903469.

Salahuddin, M.A., Al-Fuqaha, A., Guizani, M., Shuaib, K., and Sallabi, F. (2017). Softwarization of internet of things infrastructure for secure and smart healthcare. Computer *50*, 74–79.

Sasaki, J.E., Sandroff, B., Bamman, M., and Motl, R.W. (2017). Motion sensors in multiple sclerosis: narrative review and update of applications. Expert Rev. Med. Devices *14*, 891–900.

Shao, M., Han, L., Liang, J., Zhang, R., and Gao, H. (2020). A high-sensitivity liquid level sensor based on single-mode taper-thin core taper single-mode fiber structure. Meas. Sci. Technol. *31*, 105101.

Shin, Y.-E., Sohn, S.D., Han, H., Park, Y., Shin, H.-J., and Ko, H. (2020). Self-powered triboelectric/pyroelectric multimodal sensors with enhanced performances and decoupled multiple stimuli. Nano Energy *72*, 104671.

Singh, H.H., and Khare, N. (2018). Flexible zno-pvdf/ptfe based piezo-tribo hybrid nanogenerator. Nano Energy *51*, 216–222.

Song, K., Zhao, R., Wang, Z.L., and Yang, Y. (2019). Conjuncted pyro-piezoelectric effect for self-powered simultaneous temperature and pressure sensing. Adv. Mater. *31*, 1902831.

Stankovic, J.A. (2014). Research directions for the internet of things. IEEE Internet Things J. *1*, 3–9.

Tanaka, Y., Kinoshita, M., Takahashi, A., and Kurokawa, T. (2011). A wide-area sensor network based on fiber optic power supply. Jpn. J. Appl. Phys. *50*, 112501.

Tao, F., Zuo, Y., Xu, L.D., and Zhang, L. (2014). Iot-based intelligent perception and access of manufacturing resource toward cloud manufacturing. IEEE Trans. Ind. Inf. *10*, 1547–1557.

Tokuda, T., Noda, T., Sasagawa, K., and Ohta, J. (2010). Optical and electric multifunctional cmos image sensors for on-chip biosensing applications. Materials *4*, 84–102.

Tschofenig, H., and Baccelli, E. (2019). Cyberphysical security for the masses a survey of the internet protocol suite for internet of things security. IEEE Secur. Priv. *17*, 47–57.

Ullah, Z., Al-Turjman, F., Mostarda, L., and Gagliardi, R. (2020). Applications of artificial intelligence and machine learning in smart cities. Comput. Commun. *154*, 313–323.

Verma, A., Prakash, S., Srivastava, V., Kumar, A., and Mukhopadhyay, S.C. (2019). Sensing, controlling, and iot infrastructure in smart building: a review. IEEE Sens. J. *19*, 9036–9046.

Voas, J. (2016). Demystifying the internet of things. Computer *49*, 80–83.

Wang, Z.L. (2013). Triboelectric nanogenerators as new energy technology for self-powered systems and as active mechanical and chemical sensors. ACS Nano *7*, 9533–9557.

Wang, Z.L. (2015). Triboelectric nanogenerators as new energy technology and self-powered sensors - principles, problems and perspectives. Faraday Discuss. *176*, 447–458.

Wang, Z.L. (2017). On maxwell's displacement current for energy and sensors: the origin of nanogenerators. Mater. Today *20*, 74–82.

Wang, Z.L., and Song, J. (2007). Piezoelectric nanogenerators based on zinc oxide nanowire arrays. Science *312*, 242–246.

Wang, Z.L., Zhu, G., Yang, Y., Wang, S., and Pan, C. (2012). Progress in nanogenerators for portable electronics. Mater. Today *15*, 532–543.

Wang, S., Lin, L., and Wang, Z.L. (2015). Triboelectric nanogenerators as self-powered active sensors. Nano Energy *11*, 436–462.

Wang, S., Wang, Z., and Yang, Y. (2016). A one-structure-based hybridized nanogenerator for scavenging mechanical and thermal energies by triboelectric-piezoelectric-pyroelectric effects. Adv. Mater. *28*, 2881–2887.

Wang, J., Zhang, H., Xie, Y., Yan, Z., Yuan, Y., Huang, L., Cui, X., Gao, M., Su, Y., Yang, W., et al. (2017). Smart network node based on hybrid nanogenerator for self-powered multifunctional sensing. Nano Energy *33*, 418–426.

Wang, J., Xia, K., Liu, J., Li, T., Zhao, X., Shu, B., Li, H., Guo, J., Yu, M., Tang, W., et al. (2020a). Self-powered silicon pin photoelectric detection system based on triboelectric nanogenerator. Nano Energy *69*, 104461.

Wang, Z., Yu, Y., Wang, Y., Lu, X., Cheng, T., Bao, G., and Wang, Z.L. (2020b). Magnetic flap-type difunctional sensor for detecting pneumatic flow and liquid level based on triboelectric nanogenerator. ACS Nano *14*, 5981–5987.

Watral, Z., and Michalski, A. (2013). Selected problems of power sources for wireless sensors networks. IEEE Instrum. Meas. Mag. *16*, 37–43.

Wu, Z., Ding, W., Dai, Y., Dong, K., Wu, C., Zhang, L., Lin, Z., Cheng, J., and Wang, Z.L. (2018). Self-powered multifunctional motion sensor enabled by magnetic-regulated triboelectric nanogenerator. ACS Nano *12*, 5726–5733.

Wu, C., Wang, A.C., Ding, W., Guo, H., and Wang, Z. (2019a). Triboelectric nanogenerator: a foundation of the energy for the new era. Adv. Energy Mater. *9*, 1802906.

Wu, Z., Zhang, B., Zou, H., Lin, Z., Liu, G., and Wang, Z.L. (2019b). Multifunctional sensor based on translational-rotary triboelectric nanogenerator. Adv. Energy Mater. *9*, 1901124.

Xie, M., Hisano, K., Zhu, M., Toyoshi, T., Pan, M., Okada, S., Tsutsumi, O., Kawamura, S., and Bowen, C. (2019). Flexible multifunctional sensors

for wearable and robotic applications. Adv. Mater. Technol. *4*, 1800626.

Xu, G., Shi, Y., Sun, X., and Shen, W. (2019). Internet of things in marine environment monitoring: a review. Sensors *19*, 1711.

Yang, Y., Guo, W., Pradel, K.C., Zhu, G., Zhou, Y., Zhang, Y., Hu, Y., Lin, L., and Wang, Z. (2012). Pyroelectric nanogenerators for harvesting thermoelectric energy. Nano Lett. *12*, 2833–2838.

Yang, H., Liu, W., Xi, Y., Lai, M., Guo, H., Liu, G., Wang, M., Li, T., Ji, X., and Li, X. (2018). Rolling friction contact-separation mode hybrid triboelectric nanogenerator for mechanical energy harvesting and self-powered multifunctional sensors. Nano Energy *47*, 539–546.

Yang, H., Deng, M., Zeng, Q., Zhang, X., Hu, J., Tang, Q., Yang, H., Hu, C., Xi, Y., and Wang, Z. (2020). Polydirectional microvibration energy collection for self-powered multifunctional systems based on hybridized nanogenerators. ACS Nano *14*, 3328–3336.

Yu, B., and Li, H. (2019). Anonymous authentication key agreement scheme with pairing-based cryptography for home-based multi-sensor internet of things. Int. J. Distrib. Sens. Netw. *15*, 1550147719879379.

Yu, B., Yu, H., Wang, H., Zhang, Q., and Zhu, M. (2017). High-power triboelectric nanogenerator prepared from electrospun mats with spongy parenchyma-like structure. Nano Energy *34*, 69–75.

Yu, J., Hou, X., Cui, M., Zhang, S., He, J., Geng, W., Mu, J., and Chou, X. (2019). Highly skin-conformal wearable tactile sensor based on piezoelectric-enhanced triboelectric nanogenerator. Nano Energy *64*, 103923.

Zhang, Y., Jia, H., Luo, X., Chen, X., Yu, D., and Wang, R. (2003). Synthesis, microstructure, and growth mechanism of dendrite zno nanowires. J. Phys. Chem. B *107*, 8289–8293.

Zhang, Q., Liang, Q., Zhang, Z., Kang, Z., Liao, Q., Ding, Y., Ma, M., Gao, F., Zhao, X., and Zhang, Y. (2018). Electromagnetic shielding hybrid nanogenerator for health monitoring and protection. Adv. Funct. Mater. *28*, 1703801.

Zhao, S., and Zhu, R. (2018). A smart artificial finger with multisensations of matter, temperature, and proximity. Adv. Mater. Technol. *3*, 1800056.

Zhao, G., Zhang, X., Cui, X., Wang, S., Liu, Z., Deng, L., Qi, A., Qiao, X., Li, L., Pan, C., et al. (2018). Piezoelectric polyacrylonitrile nanofiber film-based dual-function self-powered flexible sensor. ACS Appl. Mater. Interfaces *10*, 15855–15863.

Zhao, R., Zhao, L., Zhang, M., Li, Z., Liu, Y., Han, T., Duan, Y., and Gao, K. (2019). Self-recovering mechanochromic luminescent material with aggregation-induced emission: implication for pressure sensor. Dyes Pigm. *167*, 181–188.

Zhao, K., Ouyang, B., Bowen, C.R., Wang, Z.L., and Yang, Y. (2020). One-structure-based multi-effects coupled nanogenerators for flexible and self-powered multi-functional coupled sensor systems. Nano Energy *71*, 104632.

Zhong, J., Zhong, Q., Chen, G., Hu, B., Zhao, S., Li, X., Wu, N., Li, W., Yu, H., and Zhou, J. (2016). Surface charge self-recovering electret film for wearable energy conversion in a harsh environment. Energy Environ. Sci. *9*, 3085–3091.

Zhu, M., Lou, M., Abdalla, I., Yu, J., Li, Z., and Ding, B. (2020a). Highly shape adaptive fiber based electronic skin for sensitive joint motion monitoring and tactile sensing. Nano Energy *69*, 104429.

Zhu, M., Lou, M., Yu, J., Li, Z., and Ding, B. (2020b). Energy autonomous hybrid electronic skin with multi-modal sensing capabilities. Nano Energy *78*, 105208.

Zianni, X. (2014). Band structure engineering in geometry-modulated nanostructures for thermoelectric efficiency enhancement. J. Electron. Mater. *43*, 3753–3757.

Zou, L., Ge, C., Wang, Z.J., Cretu, E., and Li, X. (2017). Novel tactile sensor technology and smart tactile sensing systems: a review. Sensors *17*, 2653.